

TOOLS FOR SEMI-PLANING / SEMI-DISPLACEMENT SHIP DESIGN WITH APPLICATIONS

Naval Engineering Modeling and Optimization Program (NEMO)

Report on Task 1 (Year 1) Research

Task 1: Extension of planing theory and computation to semi-planing at non-infinite Froude number.

Deliverable 1.A: Code tools for reduced gravity in bow (wave piercing) flow and increased gravity in after-hull planing flow.

Deliverable 1.B: Report on the task 1 work that includes demonstrations of the codes on modern high-speed ship forms.

to

ATI

by

William S. Vorus, PhD

School of Naval Architecture and Marine Engineering

University of New Orleans

June 20, 2005

Table of Contents	page
I. Introduction	3
II. Kinematic Boundary Condition	3
III. Linearization	5
IV. Solutions	7
V. Application	8
<i>Maruo Calculation</i>	11
<i>Michell Wave Resistance</i>	13
VI. Comparison Case	16
VII. Conclusion	18
VIII. References	19

A Combined Source-Vortex Wave Resistance Model for High-Speed Ships with Lift

I. Introduction

All surface ships or boats, regardless of size and shape, develop some circulation induced lift, and associated drag, although in many specific cases it is small. The lift may be positive or negative and is affected by wave making. The wave drag is always positive, but it has been suggested by analysis that the total drag, including circulation and the effects of gravity waves, can be reduced by the presence of wave-making, (Vorus, 2005).

Wave lift has generally been ignored in the hydrodynamic analysis of traditional ship hulls, which are characterized as “displacement hulls.” The wave drag is there predicted as from pure displacement effects, usually by the Michell-Kelvin thin ship theory (Michell, 1898). Thin ship theory has been shown to produce satisfactory wave drag results, even for shapes that would not be characterized as “thin,” e.g., (Tuck, 2002). Tuck applied Michell’s thin ship theory to a submerged spheroid and compared the results to theoretically less approximate nonlinear computations.

The primary interest here is high-speed ships, but not with speeds so high that gravity wave effects are ignorable; the interest is semi-planing/semi-displacement ships. It has traditionally been assumed that the Froude numbers of planing craft, where lift dominates buoyancy, are high enough that gravity wave effects are higher order in the hydrodynamics and can be ignored. However, even that is now questionable in view of the analysis and observations of (Vorus, 2005). At any rate, it is clear that lifting effects will be stronger in high speeds ships of the most efficient proportions. Incorporation of circulation and lift requires theoretical modeling in terms of vortices, or doublets, rather than just sources as in the non-lifting Michell theory.

II. The Kinematic Boundary Condition

Given a general floating body whose cross-section at axial position x (downstream) is depicted on Figure 1. The body geometry is defined by either of the two surface functions:

$$F_y \equiv \pm y \mp Y_0(x, z) \quad (1)$$

or

$$F_z \equiv z - Z_0(x, y) \quad (2)$$

The plus/minus signs in (1) imply that a transversely symmetric hull is assumed so that Y_0 is an odd function with respect to $y = 0$.

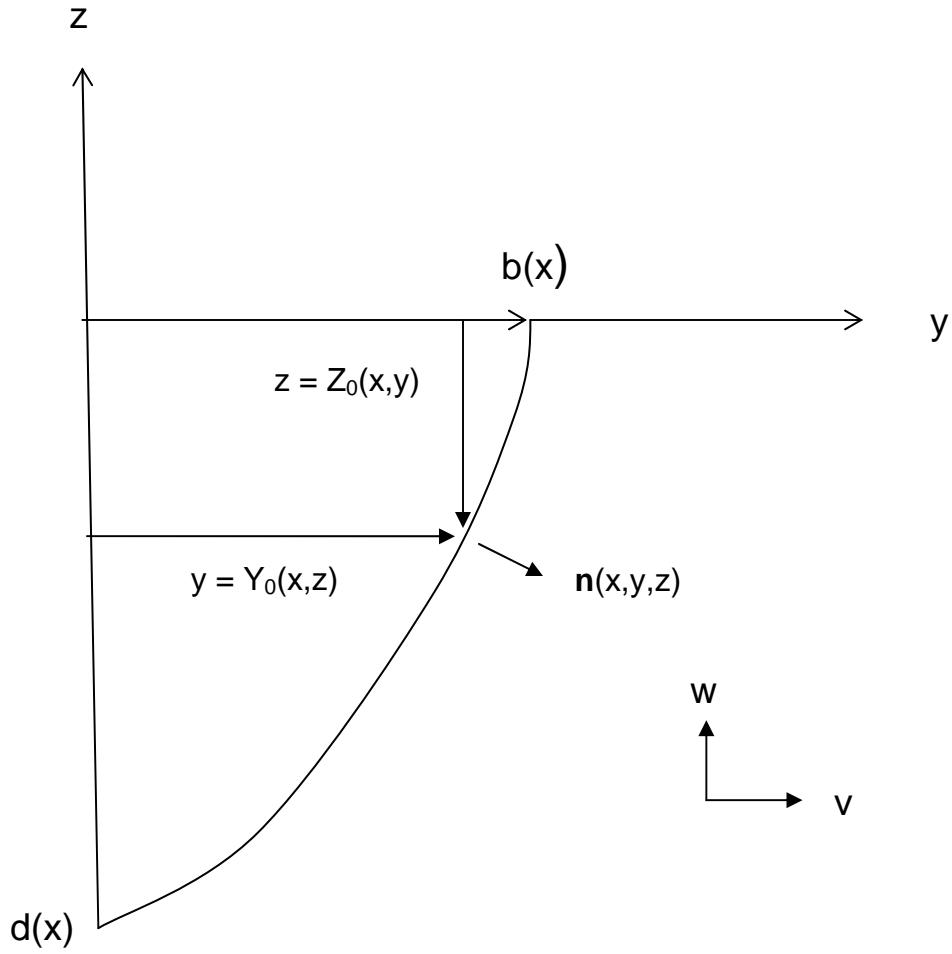


Figure1: Floating Body Cross-Section

Either of the surface definitions (1) or (2), of course, give the same unit normal vector, by the definition:

$$\bar{n} = \frac{\bar{\nabla}F}{|\bar{\nabla}F|} \quad (3)$$

for F either F_y or F_z .

The kinematic boundary condition on the body in the coordinate system translating with vessel at speed U is:

$$\bar{V} \cdot \bar{n} = 0 \quad \text{on } F = 0. \quad (4)$$

$$\text{with } \bar{V} = (U + u)\bar{i} + v\bar{j} + w\bar{k} \quad (5)$$

(4) and (5) with (1) and (2) then give two alternative, but equivalent, kinematic boundary conditions:

$$\text{From (1) and (5):} \quad \pm v \mp (U + u)Y_{0x} \mp wY_{0z} = 0 \quad \text{on } Fy = 0 \quad (6)$$

$$\text{From (2) and (5)} \quad w - (U + u)Z_{0x} \mp vZ_{0y} = 0 \quad \text{on } Fz = 0 \quad (7)$$

Since both (6) and (7) equal zero, they are equal to each other and can be superimposed to produce yet a third form of the kinematic boundary condition:

$$\pm v(x, Y_0, z) \mp [U + u(x, Y_0, z)]Y_{0x} \mp w(x, Y_0, z)Y_{0z} + w(x, y, Z_0) - [U + u(x, y, Z_0)]Z_{0x} \mp v(x, y, Z_0)Z_{0y} = 0 \quad (8)$$

$$\text{where, from Figure 1:} \quad 0 \leq x \leq \ell, \quad 0 \leq y \leq b(x), \quad -d(x) \leq z \leq 0 \quad (9)$$

Provided the sum of the terms in (8) is collectively zero for all x , y , and z specified by (9), the kinematic condition of zero normal flow on the body surface is achieved. Note that (8) is a linear sum of terms that are either odd or even in y about the vertical centerplane. (8) can therefore be re-separated into groups of even and odd terms, with both groups equal to zero.

$$\pm v(x, Y_0, z) \mp [U + u(x, Y_0, z)]Y_{0x} \mp w(x, Y_0, z)Y_{0z} \mp v(x, y, Z_0)Z_{0y} = 0 \quad (10)$$

$$w(x, y, Z_0) - [U + u(x, y, Z_0)]Z_{0x} = 0 \quad (11)$$

Now neither (10) nor (11) correspond to zero normal flow on the body boundary, but their sum, (8), does.

The evenness and oddness of the groups of terms constituting (10) and (11) is now exploited in producing approximate solutions in the same general way as the superposition used with linearized hydrofoil theory. Recall there that the section thickness offset is an odd function with respect to the meanline and the meanline camber is even. This character reduces the solution to a superposition of the independent solutions for a symmetric thickness form and a camberline of zero thickness. The symmetric thickness form, producing an odd transverse flow with no lift, is in terms of sources, and the even camberline flow, which produces the lift, is in terms of vortices.

III Linearization

For similarly superimposed flows for the ship hull case is first necessary to reduce to a lowest order (linearized) formulation by assuming that the velocity unknowns, as well as the geometry offsets and derivatives in (10) and (11) are small. Discarding the products and satisfying the resulting conditions on Y_0 and $Z_0 = 0$, respectively, gives:

$$\pm v(x, 0, z) \mp UY_{0x}(x, z) = 0 \quad (12)$$

$$w(x, y, 0) - UZ_{0x}(x, y) = 0 \quad (13)$$

(12) and (13) are the standard linearized kinematic boundary conditions for two well known approximate solutions: the odd condition (12) corresponds to a sheet of sources, $q(x, z)$, on the hull vertical centerplane, and the even condition (13) is satisfied by a sheet of transverse vortices, $\gamma_y(x, y)$, on the undisturbed waterplane. The sources produce a transverse displacement flow without circulation and lift, and the vortices produce a purely lifting flow with circulation.

The first order free-surface boundary condition, similarly linearized, accompanies both (12) and (13):

$$gw(x, y, 0) + U^2 u_x(x, y, 0) = 0 \quad (14)$$

where g is the gravitational constant.

Adding a condition of no waves propagated upstream, (12) and (14) generate “Michell’s Integral” (Michell, 1898), (Tuck, 1987) for thin ship wave resistance, and (13) and (14) correspond to Maruo’s “flat ship” theory of planing (Maruo, 1967), Vorus (2005).

The solutions to these two ideal flow boundary-value problems are to be superimposed according to the separation at (8). The model is therefore that of a slender ship which is thin, (12), but also flat (13). The schematic model “T” cross-section is depicted on Figure 2.

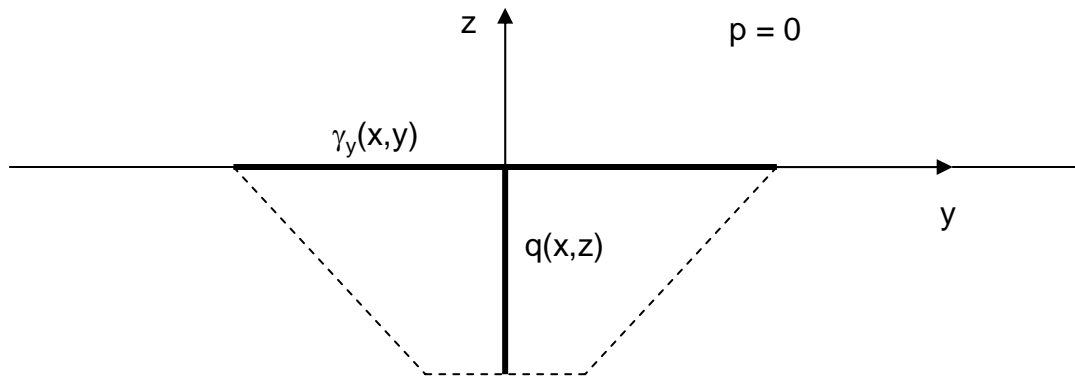


Figure 2: Thin/Flat Slender Ship Model; Sheets of Sources and Vortices

Coupling of the displacement, $q(x, z)$, and lifting, $\gamma_y(x, y)$, elements of this composite model must be addressed. The transverse vortices produce no transverse, v , normal velocities on the centerplane, so that q can be determined independently of γ_y . However, in general, the sources do produce a vertical normal velocity component on the waterplane. However, the construction of q is, from (12):

$$q(x, z) = 2UY_{0x}(x, z) \quad (15)$$

This is from two-dimensional near field solutions in x-y planes incrementally over the hull depth, which implies that flow in z is higher order. That is, a rigid wall condition with respect to the source flow over the waterplane in the near field is implicit. The two boundary value problems (12), (14) and (13), (14) are therefore uncoupled to lowest order. They can be solved independently with the corresponding solution variables simply added in achieving the complete solution.

IV Solutions

A comment on the rationale of the superimposed solutions is in order. View first from Figure 2 the case where the geometry varies only transversely in x and the transverse variation is approximately symmetric in x. In that case Z_{0x} , (13), is not zero, but it is small and produces relatively negligible lift (sinkage) forces. This describes the traditional low speed displacement ship form, where only the centerplane sources are needed to predict the far-field flow and wave resistance by Michell's Integral. On the other hand, at high speeds with hull incidence, rapid deadrise angle variations, etc, and generally asymmetric hull geometry in x, Z_{0x} is dominant and the lifting theory, (13) and (14), is needed. For fully planing craft which rise to the surface and run at shallow planing draft, only the vortex elements of the complete Figure 2 model are usually used.

The interesting situation that has stimulated the research conducted here is a need for smaller high-speed ships that may be, ideally, neither completely displacement, nor fully planing, but with some combination of the hydrodynamic features of both.

Consider then a hull form where neither Y_{0x} nor Z_{0x} are larger than the other over all regions of the surface. Then both formulations (12), (14) and (13), (14) must be solved independently over the complete hull, with the solutions then superimposed at all points.

Generalized Michell's Integral

The solution for such cases for the far-field wave resistance via Michell's Integral, (12) and (14), is straight forward; the standard model in terms of the centerplane source panels is Figure 3. The only complication here is that with transom sterns the integrated source strength does not close, and it must to satisfy continuity. This deficit is physically in the wake trough in the free-surface aft of the transom. The wake closes asymptotically to the undisturbed free surface level with increasing distance downstream. Approximate modeling is employed here by extending the centerplane source (sink) panels downstream into the wake from $x = L$ to a coordinate $x = L_w$. Over the segment $L_w - L$ the $q(x, z)$ is taken as constant and equal to $-Y_0(L, z)/(L_w - L)$. This implies a linear variation of the wake offset in x from L to closure at L_w . L_w was determined here as $L_w = 2.5L$, which is approximately the minimum value to achieve a monotonically positive asymptote of the wave resistance toward zero with increasing Fn. This is required physically.

A generalized Michell formulation is then applied as:

$$D_w = \frac{\rho U^2 v^2}{\pi} \int_{\lambda=1}^{\infty} \frac{\lambda^2}{\sqrt{\lambda^2 - 1}} (PP_1 + QQ_1) d\lambda \quad (16)$$

D_w is the wave drag, with v being the wave number, $v = g/U^2$. P, Q, P_1, Q_1 are defined as:

$$P + iQ = \int_{x=0}^L \int_{z=0}^{d(x)} q(x, z) e^{vz\lambda^2} e^{ivx\lambda} dx dz \quad (17)$$

$$P_1 + iQ_1 = \int_{x=0}^{L_w} \int_{z=0}^{d(x)} q(x, z) e^{vz\lambda^2} e^{ivx\lambda} dx dz \quad (18)$$

In (18), the source panel is extended to L_w for closure in the wake as described above. $d(x)$ is taken as constant at $d(L)$ for $L \leq x \leq L_w$.

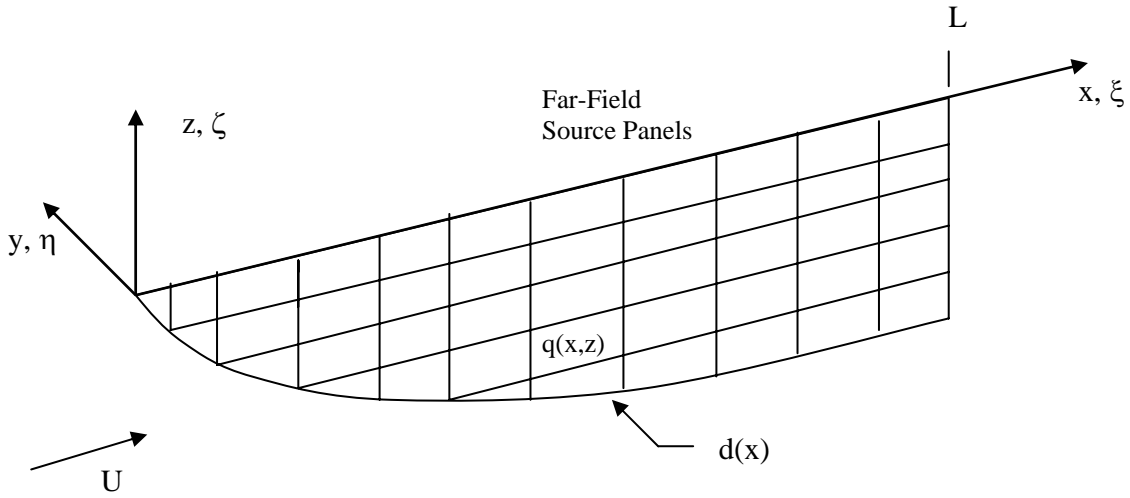


Figure 3: Source Panel Arrangement for Michell's Integral Computation

Maruo Planing Solution

The solution for the vortices on the head of the Figure 2 "T" via (13) and (14) uses the Maruo theory (Maruo, 1967), as refined and extended by Vorus (Vorus, 2005). Vorus (2005) is currently a manuscript in review for journal publication, a copy of which is included herewith as the Appendix.

V Application

Figure 4 shows the running wetted body plan of the prototype evaluation case constructed; Figure 5 is the running half-breadth, and Figure 6 is the profile. The length

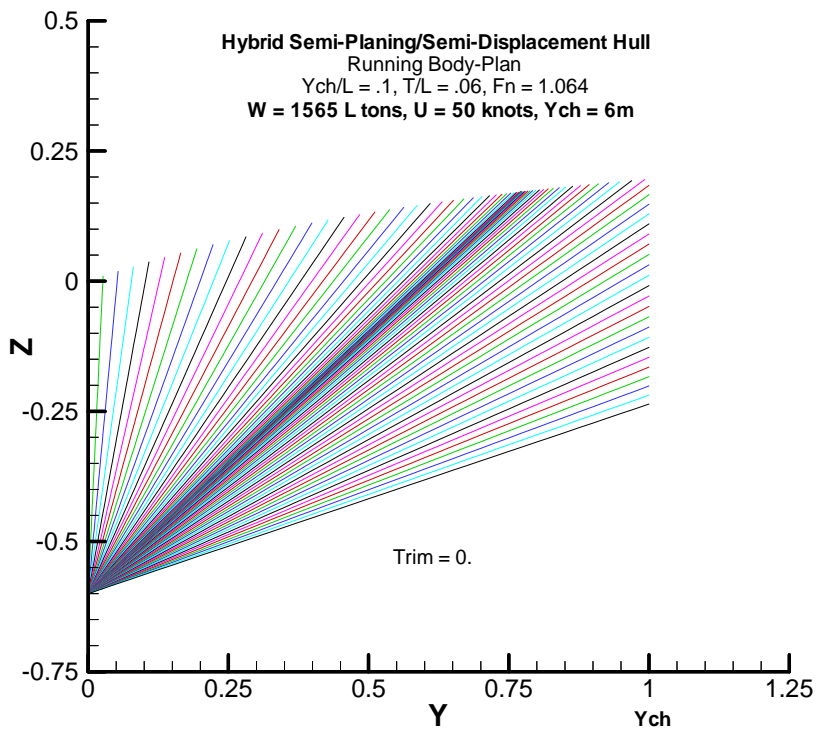


Figure 4: Running Body Plan of Prototype Vessel Selected

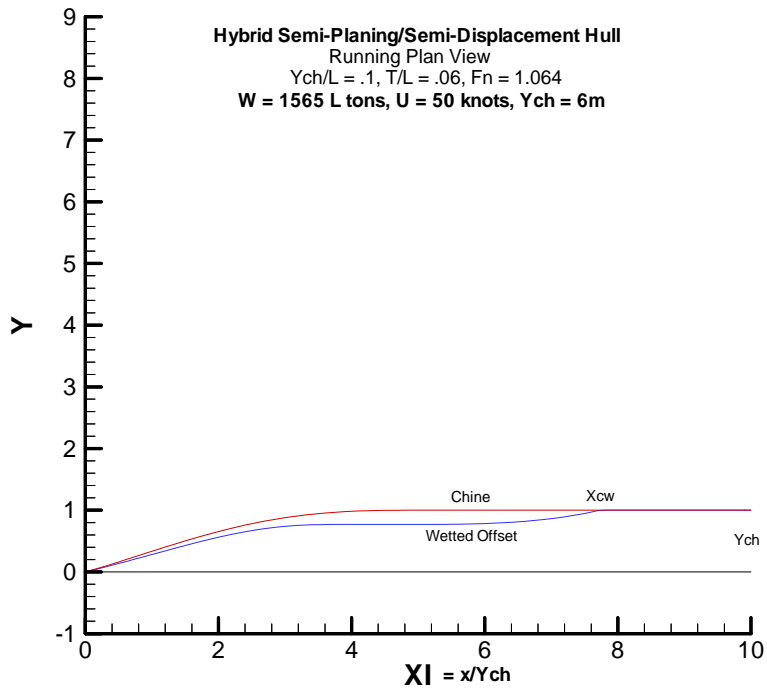


Figure 5: Running Half-Breadth Plan

of the selected vessel is 60m, with a speed of 50 knots corresponding to a Froude number, $F_n = 1.064$.

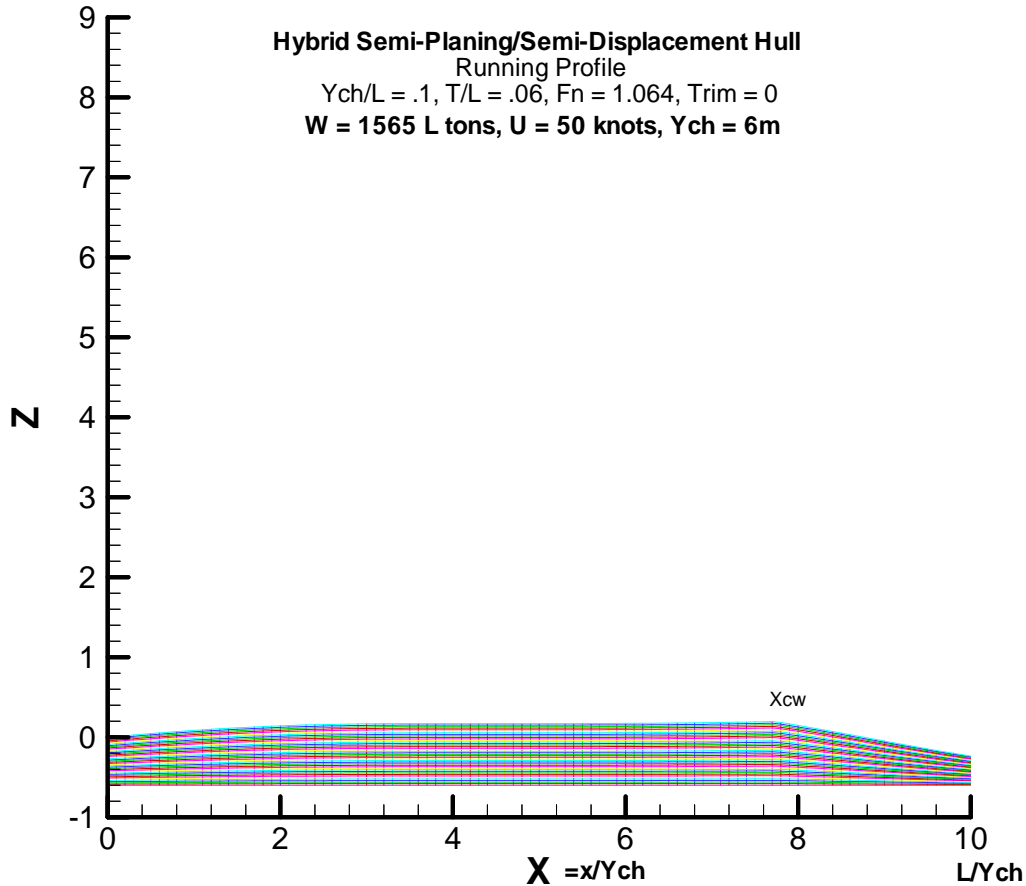


Figure 6: Running (Sub-Surface) Profile

X_{cw} indicated on Figures 5 and 6 is the chine wetting point, where the jet-head has risen up the hull sides to intersect the chine. The jet-head offset is shown on Figure 5 and lies inside (under) the chine until the intersection at X_{cw} , after which the jet-head and the chine are coincident. The implication of Figure 5 is that the hard chine is not involved with the hull surface flow until it wets at 75% of the length aft. The forebody can therefore be viewed as chineless, with the forward lines like those of a conventional fine-hulled displacement ship. Note particularly from Figures 4 and 6 that, unlike planing craft, the trim is zero consistent with displacement vessel attitude. This allows the application of a surface (or wave) piercing stem, as exhibited by Figure 6. The subsurface stem is pointed over its wetted depth.

The rapid reduction in deadrise angle, as indicated on Figure 4, and plotted specifically on Figure 7, is responsible for the rapid rise of the jet-head toward chine wetting seen in Figure 5.

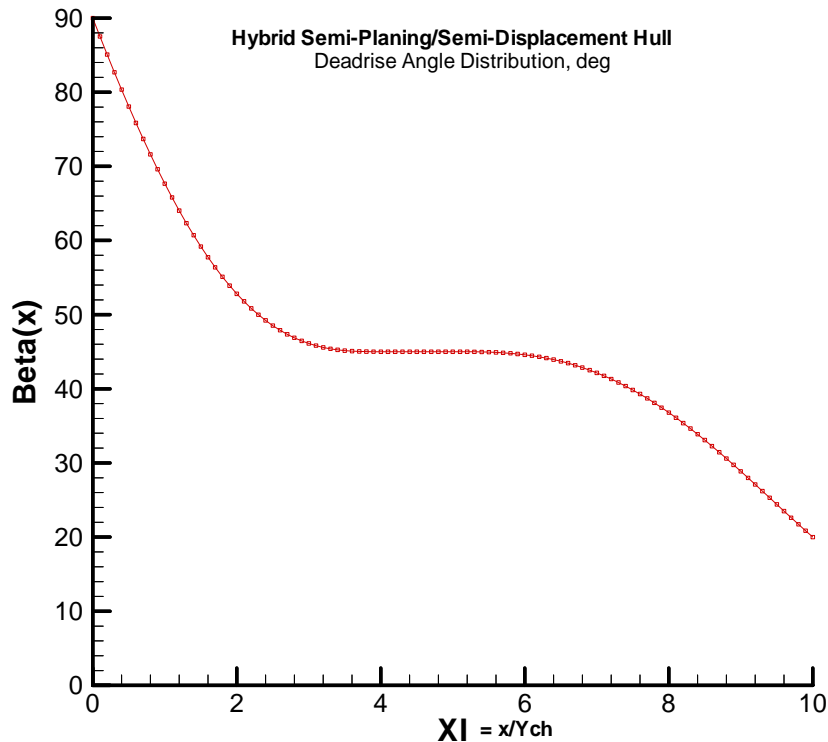


Figure 7: Deadrise Angle Distribution in x

Maruo Calculation

This high rate of deadrise reduction aft also provides the high-lift stern. The lift coefficient distribution in x over the length is shown on Figure 8. This prediction is exclusively from the vortex distribution (Figure 2) which is via the Maruo solution to (13) and (14). This theory is embodied in the new code EDITH-C¹. The centerplane source distribution, being without circulation, produces no lift. As defined in the Figure 8 caption, the coefficients are non-dimensional on vessel half-beam, rather than length. Both components of lift are included in the $C_l(x)$ of Figure 8: buoyant lift and wave lift, both of which are due to gravity. The drag curve of Figure 7 includes all of the drag components except the displacement wave drag due to the centerplane sources, Figure 2. The drag components are viscous drag, induced drag, spray drag, wave drag, and transom hydrostatic drag. The transom hydrostatic drag is due the axially unbalanced hydrostatic pressure from the wake defect associated with separation of the flow along the transom base. The viscous drag is from the ITTC friction line and is the only empiricism present in the analysis.

2 – EDITH (Engineering Development in Theoretical Hydrodynamics) - a system of computer codes and engineering procedures assembled and developed for practical application of theoretical hydrodynamics.

The center of lift is at 26.7% of the hull length forward of the transom, as noted on Figure 8. This is equivalent to the required center of gravity position for zero trim.

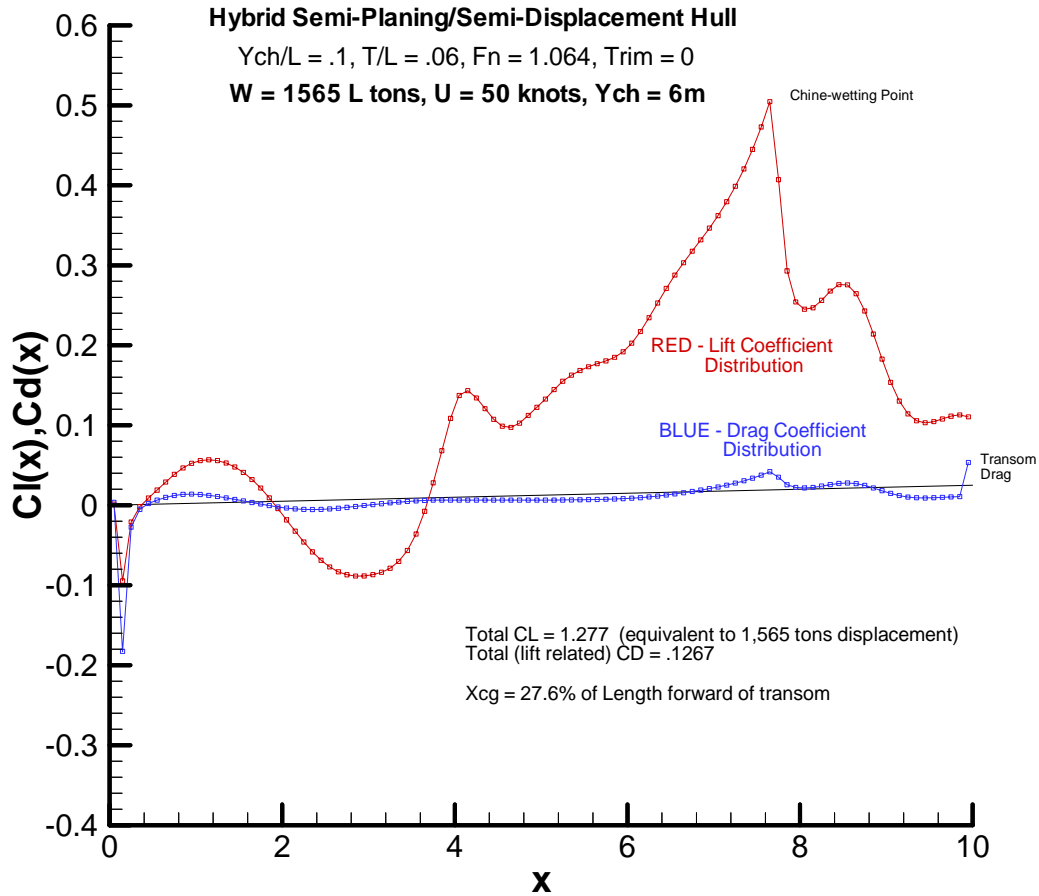


Figure 8: Lift and Drag Coefficients from Maruo theory versus x

$$C_\ell(x) = \frac{\ell(x)}{\frac{1}{2}\rho U^2 Y_{ch}^2}, \quad C_d(x) = \frac{D(x)}{\frac{1}{2}\rho U^2 Y_{ch}^2}$$

For the EDITH-C waterplane panel model the grid used had 100 elements over the length and 40 elements over the wetted transverse offset at all x. This model is shown on Figure 9. It corresponds to (both sides of) the wetted region of the projected plan of Figure 5.

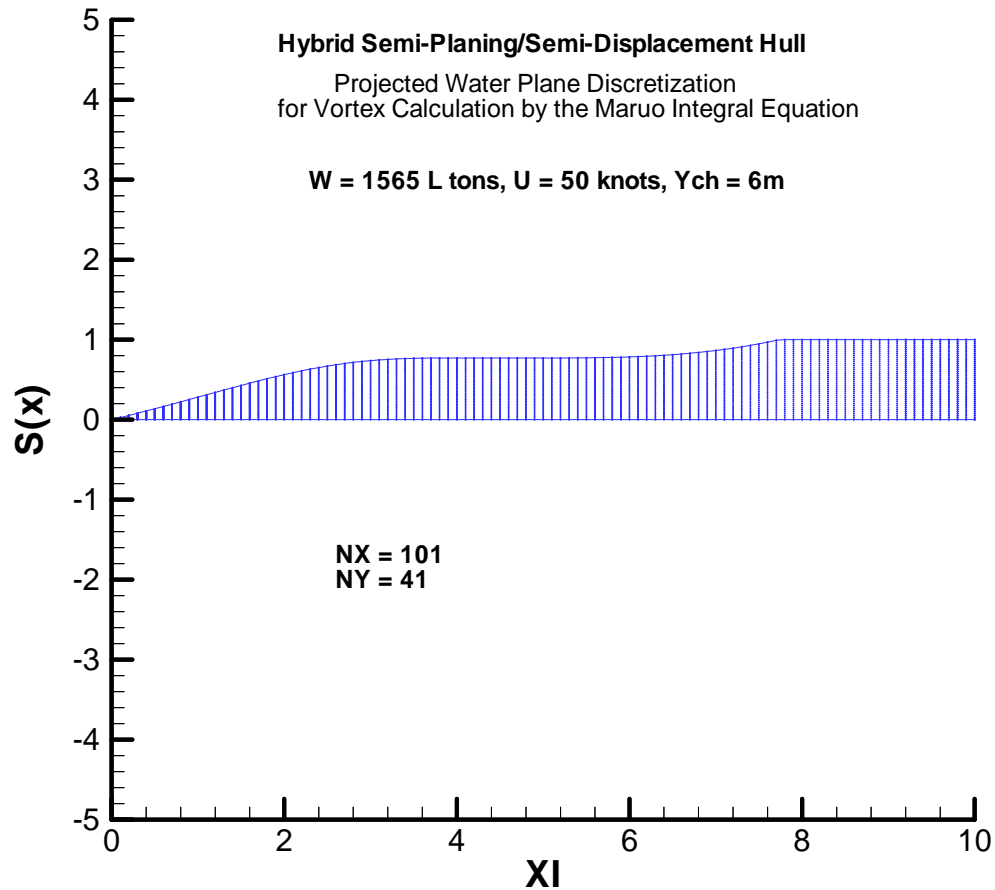


Figure 9: Projected Waterplane Discretization for Maruo Analysis

Michell Wave Resistance

The lift coefficient of Figure 8 is theoretically complete, and the drag coefficient is complete except for the wave making drag due to the centerplane sources, which is additive by the linearity of (12), (13), and (14).

The new code EDITH-D computes the source wave resistance by the generalized Michell's Integral described at (16) – (18). The centerplane discretization is shown on Figure 10, including the 150% wake extension discussed at (16). This model is composed of 100 panels in $0 - L$, and 20 panels over the draft. The body plan used for computing the $q(x,z)$ is Figure 11. Note the difference between Figure 11 and the wetted body plan, Figure 4. The Michell's integral calculation is with respect to the undisturbed water surface. Therefore, the jet-rise present on Figure 4 has been truncated on Figure 11. Also note the irregularity at the chine on Figure 11. This is a discretization error from dividing the offset into 20 equal elements at each x .

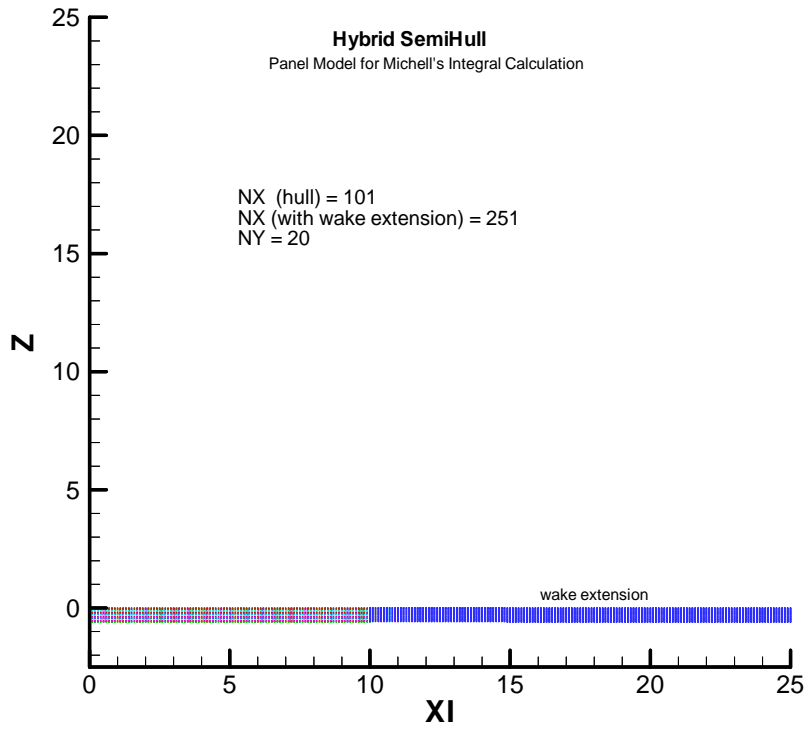


Figure 10: Panel Model for Generalized Michell's Calculation

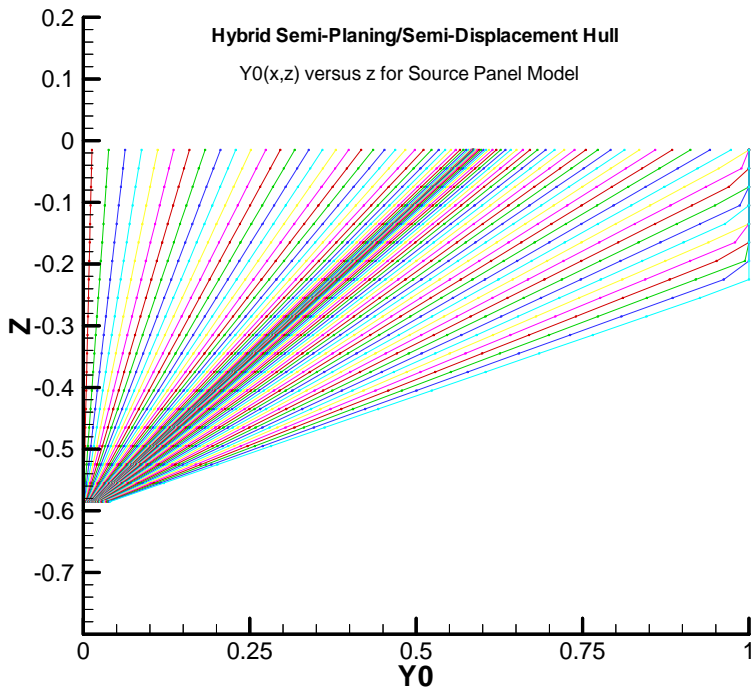


Figure 11: Body Plan for Centerplane Panelization

Figure 12 is a plot of the Michell wave resistance over a range Froude numbers that includes the design value of 1.064.

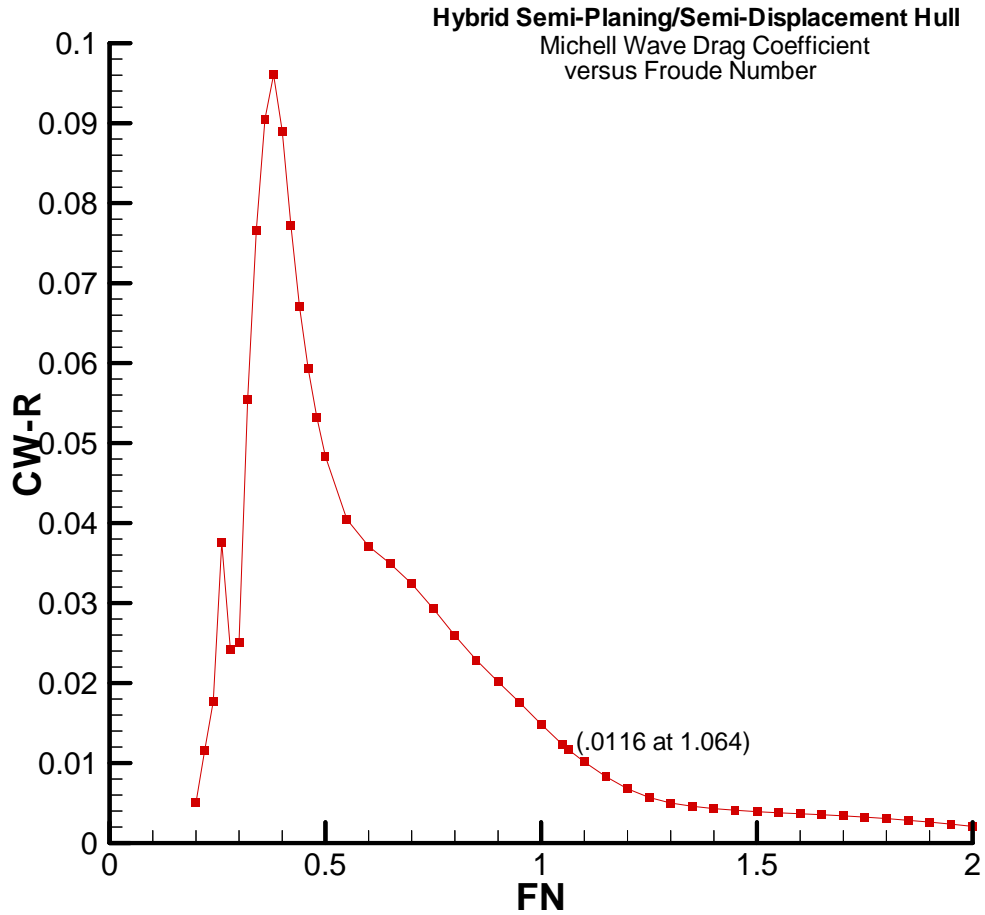


Figure 12: Michell’s Wave Resistance versus Froude Number

The non-dimensionalization on Figure 12 is the same as on Figure 8 in terms of the half-beam. The additive wave resistance coefficient is predicted as $CD-R = .0116$ at the design $F_n = 1.064$.

Table I summarizes the predicted prototype design performance after the resistance superposition.

Table I: Analysis Summary – Prototype Hybrid SemiHull Calm Water Performance

Hull length/Ych		10
Vessel operating draft/Ych		.6
Vessel operating trim, deg		0
Xcg/Ych forward of transom		2.763
Vessel speed, knots		50
Design Froude number		1.064
Hydrostatic lift at operating draft,	$\frac{\ell_b}{\frac{1}{2}\rho U^2 Y_{ch}^2}$.7780
Wave lift		.4638
Total dynamic lift		.4990
Total lift	(.7780 + .4990)	1.277
Viscous drag,	$\frac{\ell_b}{\frac{1}{2}\rho U^2 Y_{ch}^2}$.06160
Induced, spray, and transom drag		.01493
Wave drag due to waterplane wave-making vortices		.05019
Wave drag due to centerplane wave-making sources		.01164
Total Drag	(.06160 + .01493 + .05019 + .01164)	.13836
Lift/Drag Ratio	(1.277 / .13836)	9.22

VI Comparison Case

It is useful to explore the question of whether the hybrid semihull form, which develops dynamic lift but also a dynamic lift-related component of wave resistance, has the potential to compete with the non-lifting displacement hull, which develops only the one displacement component of wave resistance.

The EDITH –C and D programs have been used to re-perform the preceding analysis on a hull with lines more characteristic of a conventional displacement ship form. For this the doubly parabolic mathematical hull form was used. The wave resistance of this form has been well studied. The body plan is Figure 13. This parabolic hull was set with the same speed, length, and beam as the hybrid. However, in order to achieve the same weight a draft adjustment from T/L = .06 to T/L = .0808 was required. The trim was set to zero, giving an Xcg/L = .5 with the fore-and-aft symmetry.

The calculated wave resistances of both the parabolic hull and the hybrid SemiHull from the centerplane sources are both shown on Figure 14; the resistance for the hybrid hull is just the displacement wave resistance superimposed from Figure 12.

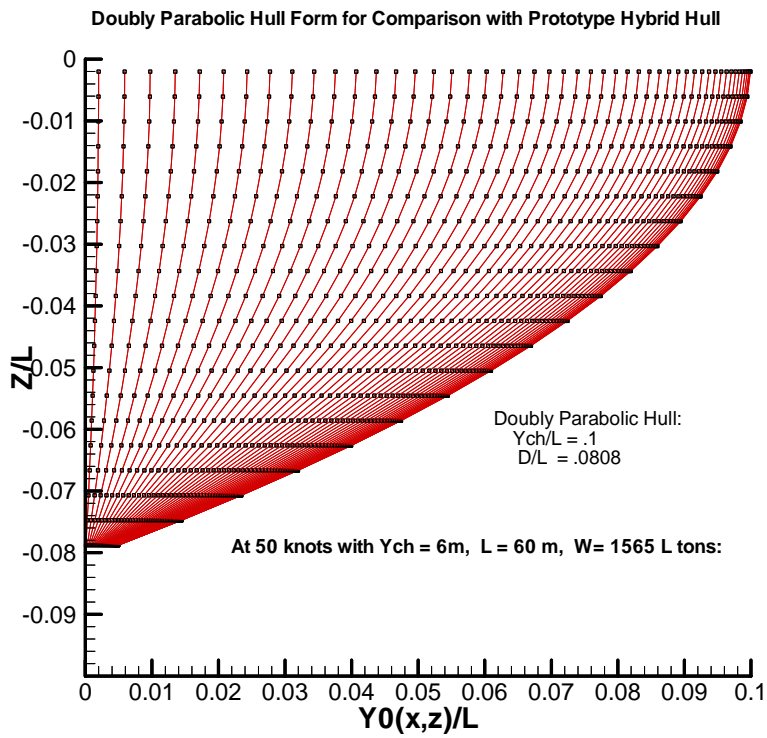


Figure 13: Body Plan of Doubly Parabolic Hull

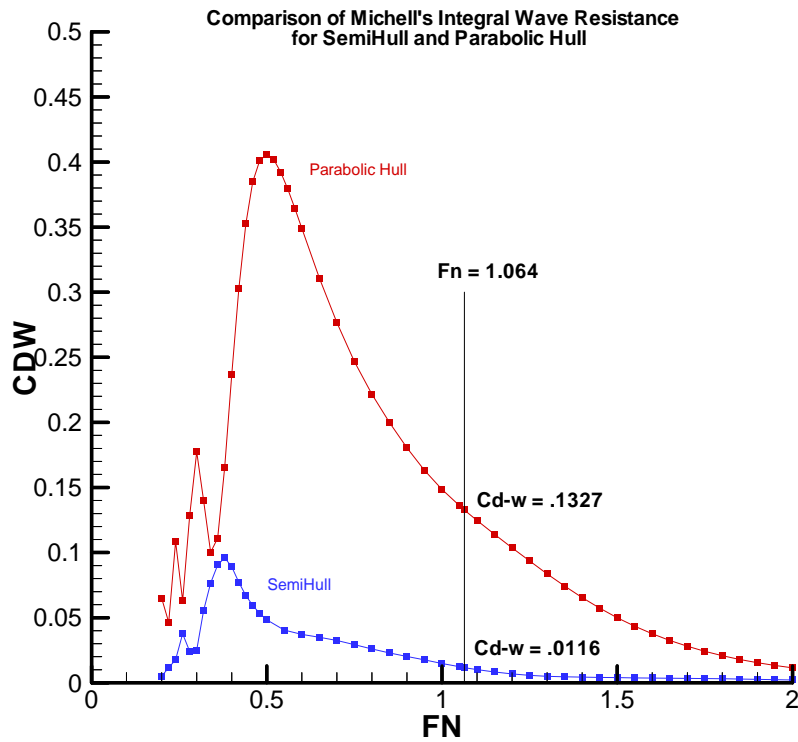


Figure 14: Michell Resistance for SemiHull and Parabolic Hull

Table 2 gives the comparison summary.

Table II – Resistance Comparison Parabolic and Hybrid SemiHulls

	Hybrid SemiHull	Parabolic Hull
Total Lift Coefficient	1.277	1.277
Viscous Drag Coefficient	.06106	.06606
Wave Drag Coefficient	.06183	.1327
Total Drag Coefficient	.13836	.19876
Lift/Drag Ratio	9.22	6.425

VII Conclusion

The comparison exhibited in Table II is not entirely fair to displacement hulls. It is well known that displacement mono-hulls of these proportions cannot be run at F_n greater than about .35 because of the prohibitively large wave resistance developing beyond that point; refer to Figure 14. Since displacement wave resistance (from centerplane sources) is proportional to beam squared, the direction taken by the naval architecture field striving for faster and faster ships is to design them to be thinner and thinner. But as the monohull becomes thinner it loses waterplane moment of inertia, as beam cubed, and encounters transverse instability. To counter the transverse instability the monohulls are expanded to multihulls: catamarans and trimarans. But with hull surface area varying most strongly with length and draft, and not beam, the viscous resistance tends to increase roughly proportional to the number of multihulls.

It can be argued based on the analysis presented here that the prevailing “band aid” approach to high speed ships may not have the potential to lead to optimum designs, at least not from the standpoint of calm-water resistance. The semi-displacement/semi-planing concept, i.e., the “SemiHull,” is suggested as a competing approach to very thin multihulls.

This is not to claim that the prototype SemiHull design evaluated here is optimum. In performing this computation it is believed, for example, that the deadrise angle distribution characteristic on Figure 7 could be improved. The high curvature entering the flat region of the deadrise distribution at XI around 2.5 is responsible for the negative lift centered at this location on Figure 8, which needs to be adjusted out. But the tools are clearly available in the EDITH system demonstrated here for optimizing the prototype SemiHull configuration.

The important point of this demonstrations and its conclusion is that a methodology has been developed and exposed for attaching the high-speed ship design effort with an

organization of established first-principles-based modeling and optimization theory and techniques. This is consistent with the fundamental goals of the ONR-NEMO program.

VIII References

Maruo, H. 1967 High and low-aspect ratio approximation of planing surfaces. *Schiffstechnik*, **72**.

Michell, J. 1898 The wave resistance of a ship. *Philosophical Magazine*, **5**, 45

Tuck, E.O., and Scullen, D.C. 2002 A comparison of linear and nonlinear computations of waves made by slender submerged bodies. *Journal of Engineering Mathematics*, 42 (2002) 255-264.

Tuck, E.O., 1987 "Wave resistance of thin ships and catamarans," The University of Adelaide, Applied Mathematics Report T8701, January

Vorus, W.S., "The importance wave-making in the lift and resistance of planing craft," submitted to the *Journal of Ship Research*, April 2005.

**TOOLS FOR SEMI-PLANING / SEMI-DISPLACEMENT SHIP
DESIGN WITH APPLICATIONS**

Naval Engineering Modeling and Optimization Program (NEMO)

Report on Task 1 (Year 1) Research

APPENDIX

The Importance of Wave-Making in the Lift and Resistance of Planing Craft

Manuscript submitted to the Journal of Ship Research

by

William S. Vorus, Professor, School of Naval Architecture and Marine Engineering,
University of New Orleans, Lake Front Campus, New Orleans, LA 70148

Ahmed Ibrahim, Graduate Student, School of Naval Architecture and Marine
Engineering, University of New Orleans

April 9, 2005

Abstract

A numerical re-formulation of Marou's integral for slender body analysis of calm-water planing hydrodynamics with gravity wave-making is developed. Numerical computations are performed first for a flat triangular planing plate. The triangular planing plate has been the subject of previous work with the base Maruo theory. The comparisons are supportive of the formulation for performing wave lift and drag calculations for realistic planing craft configurations.

An analysis is performed of the US Navy NSW 10 meter RHIB, for which some limited full scale measured data was available. Predicted boat trims versus speed are compared to measured values. The comparison is positive, even to the point of the prediction of lower speed, pre-planing "hump region" characteristics, which has never been within the reach of the traditional zero-gravity planing models.

The code written also performs the zero gravity (infinite Froude number) computation as the limiting case. This allows relative evaluation of wave effects. The remarkable prediction, in the case of the Navy RHIB, is that while a wave resistance component does occur at finite Froude number, the overall resistance with wave making is reduced relative to the zero gravity prediction. This is because the lift of the boat generated wave system produces a favorable change in the boat running attitude. The effect is reduced transom draft and reduced trim. This combines to reduce the superposition of the other resistance components of spray, induced, and viscous drag more than that added by waves.

This result is argued to be not too implausible in consideration of the different mind-set required in consideration of the hydrodynamics of planing craft, relative to that of displacement craft.

The Importance of Wave-Making in the Lift and Resistance of Planing Craft

William S. Vorus, Professor, School of Naval Architecture and Marine Engineering,
University of New Orleans

Ahmed Ibrahim, Graduate Student, School of Naval Architecture and Marine
Engineering, University of New Orleans

Introduction

Essentially all of the technology developed over the years for the analysis of planing craft hydrodynamics is a variant of, or extended from, the early work of von Karman (1929) and Wagner (1932). This includes, among others, the most notable slender body solution of Tulin (1957).

A common characteristic of the various methods of modern planing analysis has been the assumption that Froude number is high enough that gravity has negligible effect relative to convection in the fluid dynamic pressure.

Froude number for the case of a planing craft is typically defined as $F_n \equiv \sqrt{\frac{U}{gY_{ch}}}$, where

U is the vessel speed, g the acceleration of gravity, and Y_{ch} is the boat transom half-beam. In the case of displacement ships the characteristic length in the F_n is the ship waterline length; this length is not so appropriate for planing craft since the waterline length varies so dramatically with the craft loading and speed. At any rate, using the above definition, a typical operating Froude number for a planing craft at its design speed is in the range of 5 to 7. This would translate to a length-based F_n in the range of 2 to 3. For a typical displacement vessel, the speed at which wave resistance becomes prohibitively high is around a speed-length ratio of unity, which corresponds to a length Froude number of around .35. The resistance due to wave-making, however, changes as the craft begins to develop dynamic lift through the hydrodynamic planing process. The wave resistance decreases as dynamic lift begins to dominate displacement lift with the planing craft rising on the water surface. This occurs above a length Froude number approaching unity. Of course, if the craft achieves a speed less than that required for the definition of “full planing,” a semi-planing/semi-displacement state is achieved, which is currently of some interest in the development of modern high speed ships. But for “full planing” at design speed, the usual planing craft Froude number is above unity and is indeed quite high. But is it high enough to assume it to be infinite in planing boat hydrodynamic analysis? There are actually some experimental indications that it is not, with differences conjectured to be due to wave lift and drag associated with the divergent gravity wave system in the surface flow field generated by the boat¹.

1 - At planing Froude numbers the transverse wave system, relative to the diverging component, is composed of waves of length many times boat length, and is not influential in the near-field hydrodynamics.

The objective of this paper is to indicate the general importance, or unimportance, of wave-making with boats developing significant hydrodynamic lift, versus those that develop mainly displacement (buoyant) lift. This objective is engaged by comparing computations by the same theory in the limit of infinite (zero gravity) Fn , and at non-infinite Fn , for some characteristic planing craft configurations. For this purpose the starting point is taken as the base theory of Mauro(1967).

Mauro's Theory for Planing Craft Wave Making

Michell's Integral, Michell(1898), for analysis of the wave-making resistance of "thin" ships has been available for years. There, the far-field disturbance created by the ship is modeled as a sheet of fluid sources coincident with the ship vertical centerplane. This is acceptable for ships where the lift is dominated by buoyancy. But with planing craft, with the lift being dynamic lift in large part, fluid sources are not applicable (at least not alone). Either vortices or doublets are needed to capture the dynamic lifting processes.

Mauro's(1967) formulation is based on ideal flow theory and represents a solution to the Laplace equation for a velocity potential, subject to the linearized free surface boundary condition, with gravity included, and a radiation condition of no waves far upstream.

Some of Mauro's original notation is changed here for compatibility with recent work on planing.

Referring to Figure 1, x is downstream with the coordinate system located at the bow, and z is up. The planing surface is considered to occupy the region of the $z = 0$ plane corresponding to $-Y(x) \leq y \leq Y(x)$ and $0 \leq x \leq L$. The kinematic boundary condition is satisfied on this surface. The Mauro theory can therefore be considered a "flat ship" theory (Tuck, 1975), in the same sense that Michell's Integral is called "thin ship" theory. Planing craft are consistent with the assumption of flatness in satisfying boundary conditions on the $z = 0$ plane, and this has been a universal assumption for conventional analysis of planing craft at zero gravity, as built upon the original work of vonKarman' and Wagner.

Mauro reduces his general formulation in the limits of high and low aspect ratio to "thin" and "slender" bodies, respectively. It is the slender body formulation of interest here due to its applicability to planing craft. The craft must therefore have wetted geometry that can be characterized as both "flat and slender."

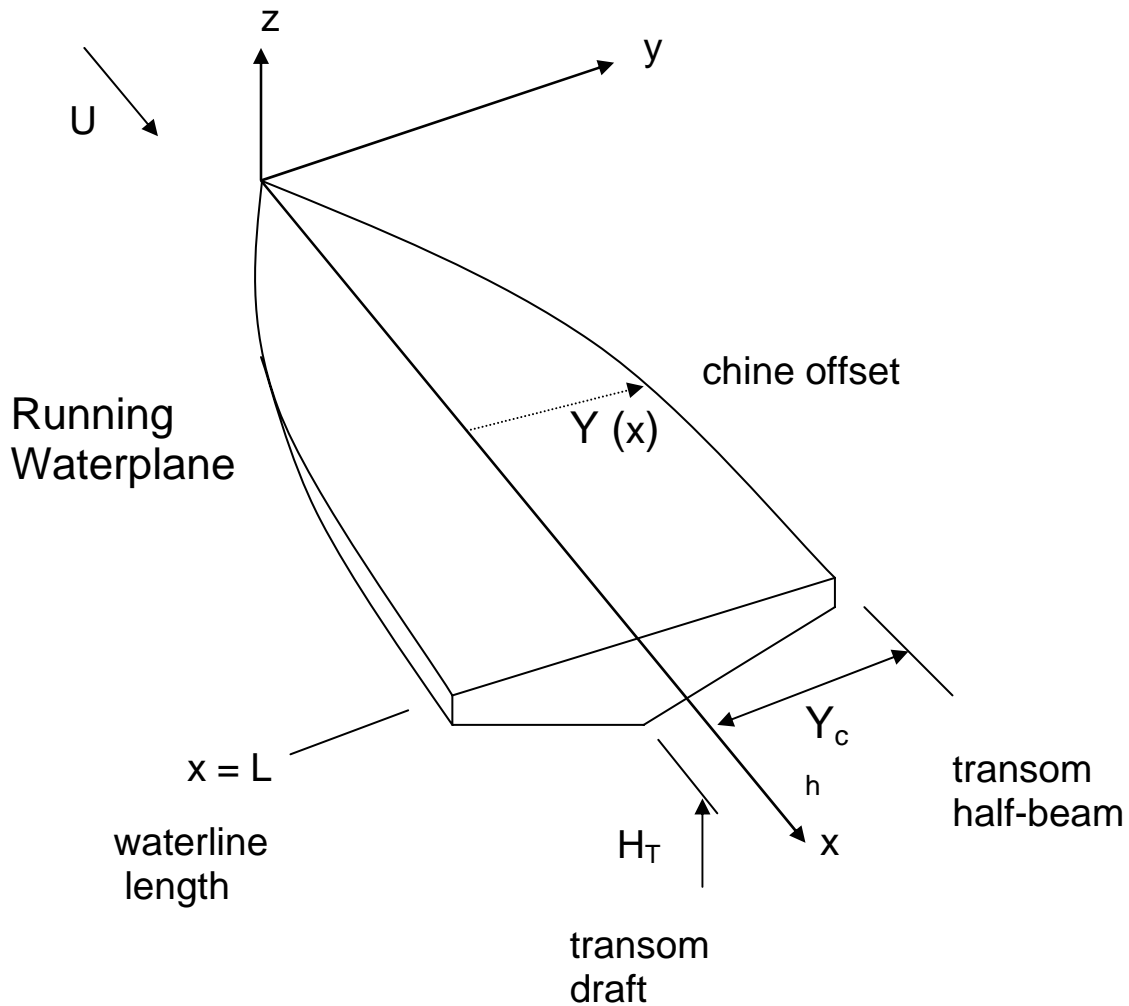


Fig. 1 Planing Boat Configuration and Coordinate System

Slender Body Theory and Formulation

The basis for slender body theory is that the gradients of both the body geometry and the flow variables are larger in the cross sectional dimensions (y and z) than in x . For consistency of order of magnitudes of the terms retained in the linearized free-surface boundary condition, it is also required that the Froude number, Fn , be large, on the order of the square-root of length-to-beam ratio. This leads to slender body equations that are parabolic in x and elliptic in the cross-sectional dimensions y and z .

The Mauro integral for a slender planing surface is from Maruo(1967), eq. (55):

$$\Phi(x, y, z) = -\frac{1}{\pi} \int_{\eta=-Y(x)}^{Y(x)} \int_{\xi=0}^x \gamma_y(\xi, \eta) \int_{\lambda=0}^{\infty} \cos[\sqrt{\kappa\lambda}(x-\xi)] \cos[\lambda(y-\eta)] e^{\lambda z} d\lambda d\xi d\eta \quad (1)$$

Here, referring to Figure 1, Φ is the velocity potential in the fluid region $z \leq 0$. γ_y is the unknown transverse (y-directed) vortex density component on the planing surface. The companion axial vortex density component, γ_x , is the usual subject of the conventional zero gravity slender body formulation of planing, but the two components are related by the condition of zero divergence of the two dimensional surface vector.

κ in (1) is the wave number $\kappa = g/U^2$ and is present from the derivation (1) in satisfying the linearized free surface boundary condition, allowing for gravity wave generation.

Note from (1) that only the sections at $\xi < x$ upstream convect into the current x – solution section; γ_y for $\xi < x$ will always be known from upstream computation steps. This x-marching characteristic of elliptic solutions in the y-coordinate is common to the parabolic reduction in x associated with all slender body theories.

The linearized kinematic boundary condition on the planing surface is:

$$\frac{\partial \Phi}{\partial z} = U \frac{\partial z_0}{\partial x} \quad \text{on } z = 0, \quad -Y(x) \leq y \leq Y(x), \quad 0 \leq x \leq L \quad (2)$$

Here $z_0(x, y)$ is the definition of the planing surface $z - z_0(x, y) = 0$, which is presumed to be known.

Nondimensionalize velocities on U and dimensions on the transom chine-half-beam Y_{ch} , and denote derivatives by subscripts. (2) then becomes, with (1), for $z \rightarrow 0$:

$$z_{0,x}(x, y) = \frac{1}{\pi} \int_{\eta=-Y(x)}^{Y(x)} \int_{\xi=0}^x \gamma_y(\xi, \eta) \int_{\lambda=0}^{\infty} \cos\left[\frac{\sqrt{\lambda}}{F_n}(x-\xi)\right] \cos[\lambda(y-\eta)] \lambda e^{\lambda z} d\lambda d\xi d\eta \quad (3)$$

With this non-dimensionalization, the Froude number appearing in (3) is:

$$F_n \equiv \frac{U}{\sqrt{gY_{ch}}} . \quad (4)$$

Since the boundary conditions are being satisfied on the $z = 0$ plane, z should be set to zero in (3). However, while the resulting equation can then be integrated in terms of special functions, a non-obvious essential singularity results in the 2-D sectional-y solutions that produces non-convergent results. Maruo(1967) very indirectly implied recognition of this difficulty in his general formulation. Later, Tuck(1975), pursued Maruo's integral equation (with z set to 0 in (3)). Tuck recognized the singularity problem and showed it very succinctly, but was still not satisfied that he had dealt with it effectively in achieving stable, convergent numerical predictions. Later, Cole (1988), in seeming frustration over the apparent numerical intractability of (3) (with $z = 0$),

developed an analytic solution for a very special case. That contribution can be considered a significant achievement, but is not of much practical value.

The key to achieving a valid numerical solution to (3) has been found here to be to first proceed with the discrete integration of (3) with arbitrary z less than zero, and then to carefully execute the limiting process $z \rightarrow 0$. This is developed in the appendix and adapted in the following.

Slender Body Solution

First further non-dimensionalize (3) locally on $Y(x)$ and collapse the solution domain to the positive y -axis. There results:

$$z_{0x}(x, y) = \frac{Y(x)}{\pi} \int_{\eta=0}^1 \int_{\xi=0}^x \gamma_y(\xi, \eta) \int_{\lambda=0}^{\infty} \cos[\sqrt{\lambda} / F_n(x - \xi)] \{ \cos[\lambda Y(x)(y - \eta)] + \cos[\lambda Y(x)(y + \eta)] \} \lambda e^{\lambda z} d\lambda d\xi d\eta \quad (5)$$

Now consider the x and y domains of (5) discretized into nx and Ny elements, respectively. Ny is fixed for all x with the Ny elements distributed in $0 \leq y \leq 1$. nx progresses from 1 to Nx with an additional element added as x progresses in the Nx steps. $\gamma_y(x, y)$ is approximated as piecewise constant over the elements as $\bar{\gamma}_{yij}$, $i = 1, \dots, nx$, $j = 1, \dots, Ny$. Integration is then piecewise in both the ξ and η variables on the right-hand-side of (5) to form a double series with nx and Ny terms in each:

$$z_{0x}(x, \bar{y}) = \frac{F_n}{\pi} \sum_{j=1}^{Ny} \sum_{i=1}^{nx} \bar{\gamma}_{yij} \int_{\lambda=0}^{\infty} \sin \frac{\sqrt{\lambda}}{F_n} (x - \xi) \Big|_{\xi=\xi_i}^{\xi_{i+1}} \left[\sin \lambda Y(x)(\bar{y} - \eta) - \sin \lambda Y(x)(\bar{y} + \eta) \right]_{\eta=\eta_j}^{\eta_{j+1}} e^{\lambda z} \frac{d\lambda}{\sqrt{\lambda}} \quad (6)$$

with $nx = 1, \dots, Nx$. This step is similar to that executed in Tuck (1975). The over-bars in (6) imply values at element mid-points, whereas ξ_i and η_j are at the element ends; x in (6) corresponds to ξ_{nx+1} . x is fixed at the value of ξ_{nx+1} during the summation of all upstream $\bar{\gamma}_{yij}$, 1 to nx , which are known at any computation step. nx increases by 1 with each computation step up to Nx , with $Nx+1$ corresponding to $x = L$ (Figure 1).

Equation (6) can be written for solution as,

$$z_{0x}(x, \bar{y}) = \frac{F_n}{\pi} \sum_{j=1}^{Ny} \sum_{i=1}^{nx} \bar{\gamma}_{yij} I_{\lambda}(x, \bar{y}, \xi, \eta) \Big|_{\xi=\xi_i}^{\xi_{i+1}} \Big|_{\eta=\eta_j}^{\eta_{j+1}} \quad (7)$$

where I_{λ} is the improper λ -integral in (6). Write I_{λ} as the sum of two integrals corresponding to the two sine-terms in (6).

$$I_{\lambda} = I_{\lambda}^{-} - I_{\lambda}^{+} \quad (8)$$

where the $-$ and $+$ signs correspond to those in (6). It is I_{λ}^{-} for which care must be exercised with the higher order singularity in y . z can, however, be set to zero in I_{λ}^{+} in advance and the integral performed directly in terms of Fresnel Integrals (Gradshteyn and Ryzhik (1965)) as:

$$I_{\lambda}^{+}(x, \bar{y}, \xi, \eta) \equiv \sqrt{\frac{\pi}{2}} \frac{1}{a_{+}} \left[\cos\left(\frac{b^2}{a_{+}^2}\right) C\left(\frac{b}{a_{+}}\right) + \sin\left(\frac{b^2}{a_{+}^2}\right) S\left(\frac{b}{a_{+}}\right) \right] \quad (9)$$

With some care, I_{λ}^{-} can be expressed as developed in the Appendix in the similar form:

$$I_{\lambda}^{-}(x, \bar{y}, \xi, \eta) \equiv \text{sgn}(\bar{y} - \eta) \sqrt{\frac{\pi}{2}} \frac{1}{a_{-}} \left[\cos\left(\frac{b^2}{a_{-}^2}\right) C\left(\frac{b}{a_{-}}\right) + \sin\left(\frac{b^2}{a_{-}^2}\right) S\left(\frac{b}{a_{-}}\right) \right] e^{-\frac{z}{a_{-}} \left(\frac{b}{a_{-}}\right)^2} \quad (10)$$

where, in (9) and (10): $b = b(x, \xi) \equiv \frac{x - \xi}{2F_n}$ and $a_{+}(x, \bar{y}, \eta) \equiv \sqrt{Y(x)|\bar{y} + \eta|}$
 $a_{-}(x, \bar{y}, \eta) \equiv \sqrt{Y(x)|\bar{y} - \eta|} \quad (11)$

Numerical convergence in the troublesome I_{λ}^{-} term is provided by the exponential factor in (10); see Tuck(1975) and the Appendix for elucidation of the difficulty. Here z is selected so that $\frac{z}{a_{-}^2} \ll 1$. The maximum value of this factor occurs at the minimum of $Y(x)\Delta\eta_j/2$ such that z can be taken arbitrarily as $z \ll Y(x) \min(\Delta\eta_j)/2$ for computational purposes; a value of $z(x) = \varepsilon Y(x) \min(\Delta\eta_j)$ with ε on the order of $\varepsilon = .1$ to $.2$ is found to be appropriate.

This convergence factor can actually be applied to both sets of terms originating at (5) without any loss of function. For $\bar{y} + \eta$, or for $\bar{y} - \eta$ with $\bar{y} \neq \bar{y}_j$, or for $b \rightarrow 0$, the exponential argument is small, such that minimum reduction occurs where none is needed.

Solution for Numerical Analysis

Return to the solution equation (7) with $I_{\lambda}(x, \bar{y}, \xi, \eta)$ now evaluated for effective numerical analysis.

In (7), the contributions from the first downstream element row bounded by x , i.e., $\xi_{nx} \rightarrow x$, should have no wave effects. This can be deduced by first observing that $b(x, \xi)$ in (10) is small for $x - \xi$ small, and F_n not small. Small b produces the following

asymptotic form of I_λ in (7). For small b the terms in (7), by (9) and (10), are dominated by the Fresnel integral C , which is to first order for small argument:

$$C \left[\frac{(x - \xi)}{2F_n \sqrt{Y(x)} |\bar{y} \pm \eta|} \right] \rightarrow \frac{1}{\sqrt{2\pi}} \frac{(x - \xi)}{F_n \sqrt{Y(x)} |\bar{y} \pm \eta|} \quad (12)$$

Substitution of (12) into I_λ of (7) gives, to lowest order, with $\cos \rightarrow 1$. and $\sin \approx S \rightarrow 0$:

$$z_{0x}(x, \bar{y}) = -\frac{1}{\pi} \frac{\Delta x_{nx}}{Y(x)} \sum_{j=1}^{N_y} \bar{\gamma}_{yNxj} \left(\frac{\eta}{\bar{y}^2 - \eta^2} \right) \Big|_{\eta=\eta_j}^{\eta_{j+1}} + \frac{F_n}{\pi} \sum_{j=1}^{N_y} \sum_{i=1}^{nx-1} \bar{\gamma}_{yij} I_\lambda(x, \bar{y}, \xi, \eta) \Big|_{\xi=\xi_i}^{\xi_{i+1}} \Big|_{\eta=\eta_j}^{\eta_{j+1}} \quad (13)$$

With all of the $\bar{\gamma}_{yij}$ known up through $i = nx-1$, the solution to (13) is therefore from:

$$RHS_k(x) = \sum_{j=1}^{N_y} \bar{\gamma}_{yNxj} C_{jk}(x) \quad (14)$$

where: $\bar{y} \equiv \bar{y}_k$ and, from (13):

$$RHS_k(x) \equiv z_{0x}(x, \bar{y}_k) - \frac{F_n}{\pi} \sum_{j=1}^{N_y} \sum_{i=1}^{nx-1} \bar{\gamma}_{yij} I_\lambda(x, \bar{y}_k, \xi, \eta) \Big|_{\xi=\xi_i}^{\xi_{i+1}} \Big|_{\eta=\eta_j}^{\eta_{j+1}} \quad (15)$$

The inversion needed in (14) and (15) can actually be converted analytically via the exact inverse used by Maruo(1967). This is:

$$\bar{\gamma}_{yNxk} = \frac{Y(x)}{\pi \Delta x_{nx}} \sum_{j=1}^{N_y} R\bar{H}S_j \int_{\eta=\eta_j}^{\eta_{j+1}} \ell n \left| \frac{\left\{ \left[1 + \sqrt{(1 - \bar{y}_k^2)(1 - \eta^2)} \right]^2 - \eta^2 \bar{y}_k^2 \right\}}{\eta^2 - \bar{y}_k^2} \right| d\eta \quad (16)$$

$$\text{with, in (16): } R\bar{H}S_j \equiv z_{0x}(x, \bar{\eta}_j) - \frac{F_n}{\pi} \sum_{j=1}^{N_y} \sum_{i=1}^{nx-1} \bar{\gamma}_{yij} I_\lambda(x, \bar{\eta}_j, \xi, \eta) \Big|_{\xi=\xi_i}^{\xi_{i+1}} \Big|_{\eta=\eta_j}^{\eta_{j+1}} \quad (17)$$

Formula (16) can be integrated semi-analytically for subsequent numerical analysis as:

$$\begin{aligned} \bar{\gamma}_{yNxk} = & \frac{Y(x)}{\pi \Delta x_{nx}} \sum_{j=1}^{N_y} R\bar{H}S_j \left\{ \ell n \left[\left(1 + \sqrt{(1 - \bar{y}_k^2)(1 - \bar{\eta}_j^2)} \right)^2 - \bar{y}_k^2 \bar{\eta}_j^2 \right] \eta - (\eta + \bar{y}_k) \ell n(\eta + \bar{y}_k) - \right. \\ & \left. - (\eta - \bar{y}_k) \ell n|\eta - \bar{y}_k| + 2\eta \right\} \Big|_{\eta=\eta_j}^{\eta_{j+1}} \quad (18) \end{aligned}$$

Infinite F_n Reduction

The step at (13) which evaluated the first term on the basis of small argument of the Fresnel integrals can be extended to all of the x -terms in the series (19) at very large F_n , in reconsideration of (12). That is, in the case of $F_n \rightarrow \text{large}$ all of the x -series terms in (13) are small. In this case, (13) can be written:

$$z_{0x}(x, y) = -\frac{1}{\pi} \frac{1}{Y(x)} \sum_{j=1}^{N_y} G_{Ij} \left(\frac{\eta}{\bar{y}^2 - \eta^2} \right) \Big|_{\eta=\eta_j}^{\eta_{j+1}} \quad (19)$$

where G_{Ij} is the spanwise circulation of the lifting surface up to x :

$$G_{Ij} \equiv \sum_{i=1}^{nx} \bar{\gamma}_{lyij} \Delta x_i \equiv \sum_{i=1}^{nx} \Delta G_{lij} \quad (20)$$

The infinite- F_n G_{Ij} are therefore available from the same inverse (16):

$$G_{Ik} = \frac{Y(x)}{\pi} \sum_{j=1}^{N_y} z_{0x}(x, \eta_j) \int_{\eta=\eta_j}^{\eta_{j+1}} \ell n \left| \frac{\left\{ \left[1 + \sqrt{(1 - \bar{y}_k^2)(1 - \eta^2)} \right]^2 - \eta^2 \bar{y}_k^2 \right\}}{\eta^2 - \bar{y}_k^2} \right| d\eta \quad k = 1, \dots, N_y \quad (21)$$

with the γ_{lyij} by numerical differentiation of this result, using (20):

$$\bar{\gamma}_{lyij} = \frac{\Delta G_{lij}}{\Delta x_i} \quad (22)$$

Another alternative is just to write $RHS_k(x)$ at (15) in terms of the infinite F_n I_λ and compute γ_{lyij} term by term as with the finite F_n calculation by (18). That is, in (17):

$$RHS_{Ij} \equiv z_{0x}(x, \bar{\eta}_j) + \frac{1}{\pi} \sum_{j=1}^{N_y} \sum_{i=1}^{nx-1} \bar{\gamma}_{lyij} \Delta x_i \left(\frac{\eta}{\bar{y}^2 - \eta^2} \right) \Big|_{\eta=\eta_j}^{\eta_{j+1}} \quad (23)$$

with substitution of (23) into (18) to achieve γ_{lyij} .

Pressure, Lift, and Drag

With $\gamma_y(x, y)$ known by the preceding solution, the Bernoulli equation gives the planing surface pressure:

$$p(x, y, z) + \rho gz + \frac{1}{2} \rho \left\{ [U + u(x, y)]^2 + v(x, y)^2 + w(x, y)^2 \right\} \quad (24)$$

Linearize (24) and evaluate the result on $z = 0$. This gives:

$$p(x, y) = -\rho U u(x, y) \quad \text{on } z = 0 \quad (25)$$

The coefficient of pressure difference across the surface is then:

$$C_p(x, y) \equiv \frac{p(x, y)}{\frac{1}{2} \rho U^2} \quad (26)$$

Substitute (25) into (26):

$$C_p(x, y) = -2 \left(\frac{u}{U} \right) \quad (27)$$

Considering all velocity quantities henceforth dimensionless on U , $u(x, y)$ is written on the planing surface in terms of the vortex strength γ_y as:

$$u(x, y) = -\gamma_y(x, y) \quad (28)$$

The pressure coefficient, from (27), is then just:

$$C_p(x, y) = 2\gamma_y(x, y) \quad (29)$$

The sectional lift coefficient is given in terms of (29) as:

$$C_\ell(x) \equiv \frac{\ell(x)}{\frac{1}{2} \rho U^2 Y(x)} = 2 \int_{y=0}^1 C_p(x, y) dy = 4 \int_{y=0}^1 \gamma_y(x, y) dy \quad (30)$$

The total lift coefficient is:

$$C_L = \frac{L}{\frac{1}{2} \rho U^2 Y_{ch}^2} = \int_{x=0}^L C_\ell(x) Y(x) dx \quad (31)$$

The sectional drag is the sectional integral of the axial projection of the surface pressure:

$$C_d(x) \equiv \frac{d(x)}{\frac{1}{2} \rho U^2 Y(x)} = 2 \int_{y=0}^1 C_p(x, y) z_{0x}(x, y) dy = 4 \int_{y=0}^1 \gamma_y(x, y) z_{0x}(x, y) dy \quad (32)$$

The total drag coefficient follows as by (31):

$$C_D = \frac{D}{\frac{1}{2}\rho U^2 Y_{ch}^2} = \int_{x=0}^L C_d(x) Y(x) dx \quad (33)$$

Evaluation

The Maruo theory has been applied to a flat triangular flat plate on at least two previous occasions: Marou(1967) and Tuck(1975). The triangular planing plate, Figure 2, therefore serves as a comparative basis for checking the general slender-body planing theory assembled here.

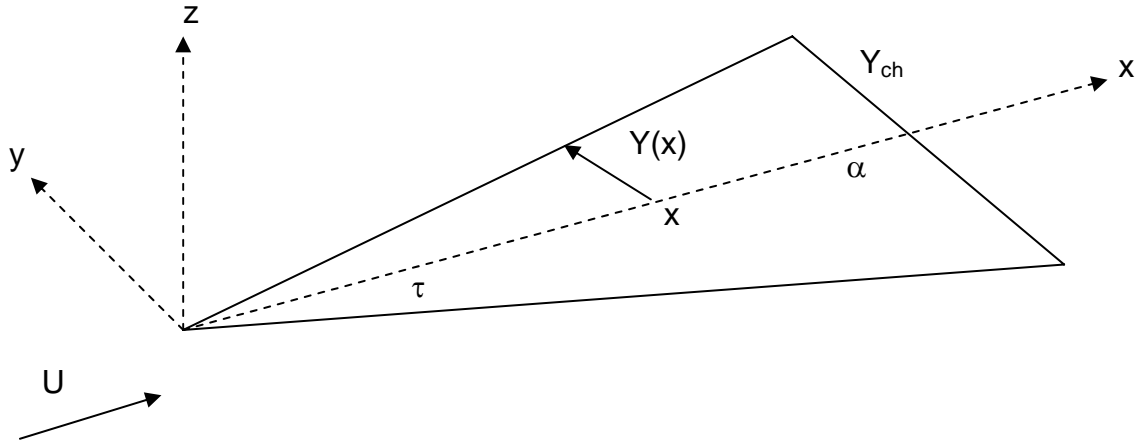


Figure 2: Flat Triangular Planing Plate

Maruo(1967) never actually solved his integral equation; he said it was too difficult. As previously noted in the introduction, it is inherent in the slender body formulation that,

for validity, the Froude number must be high, $F_n = O\left(\sqrt{\frac{L}{Y_{ch}}}\right)$. Maruo produced an

asymptotic approximation by requiring the Froude number to be *very* high:

$\frac{1}{F_n} \sqrt{\frac{L}{Y_{ch}}} = o(1)$. This allowed Maruo to substitute the infinite F_n solution, $\gamma_y(x,y)$, by

(21) and (22), with the full kernel of (3) to calculate a correction for wave effects.

Tuck(1975) did solve the full equation, but he was pessimistic about his numerical analysis being poorly conditioned due to the higher order singular behavior in y . That appears to have led to some questionable projections by Tuck.

Tuck claimed to have identified from his numerical analysis a singularity in pressure along the plate centerline. Figure 3 is a plot, by the current analysis, for a plate with a

half-apex angle of 10 degrees. It is of $\gamma_y(x,y)/\tan(\alpha)$ by (18) versus $\eta = y/Y(x)$ for overlays at the 100 stations in x . The curves can, of course, be multiplied by any $\tan(\alpha) \approx \alpha$ since the theory is linear on small incidence.

The half-beam Froude number of Figure 3 is 4.0, with a corresponding length $Fn = 1.7$. The inner (lower) curve on Figure 3 is at station 1 at the apex, which corresponds to an infinite- Fn flow. This is the well known semi-elliptic shape from low-aspect-ratio wing theory. The companion $\gamma_x(x,y)$ will be square-root singular along the leading edge. Here, the γ_y -curves do peak just inboard of the edge and then drop ever more steeply to zero at the edge with increasing distance downstream as the wave effects amplify. The y -discretization represented the half-width at all x by 40 elements of equal length in y .

The increasing height of the curves on Figure 3 corresponds to increasing x downstream and increasing wave flow effects. With the pressure coefficient being twice γ_y from (29), there is no evidence of a pressure singularity along the plate centerline from these calculations (and there is no obvious theoretical reason that there should be).

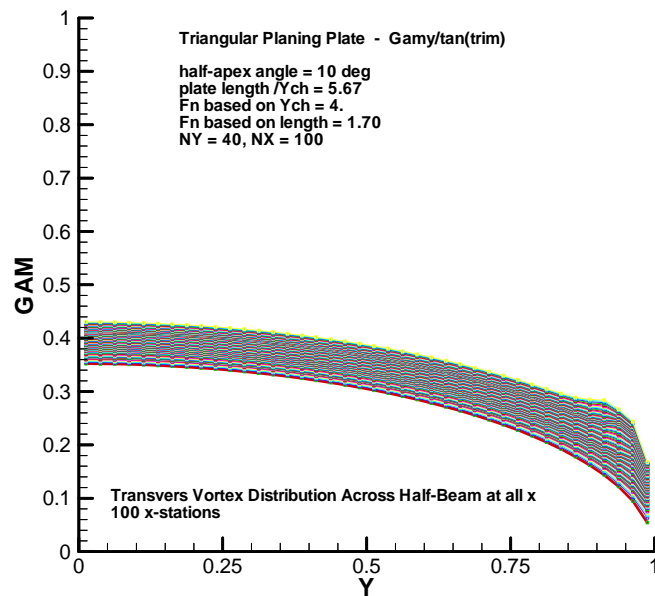


Figure 3: Sectional $\gamma_y(x,y)$ at all x -stations

This is supported by Figure 4, which is a plot, for the same 10 deg plate of Figure 3, of $\gamma_y(x,y)$ versus x for $\eta = y/Y(x) = .0125$ (the center of the first element) off the plate centerline.

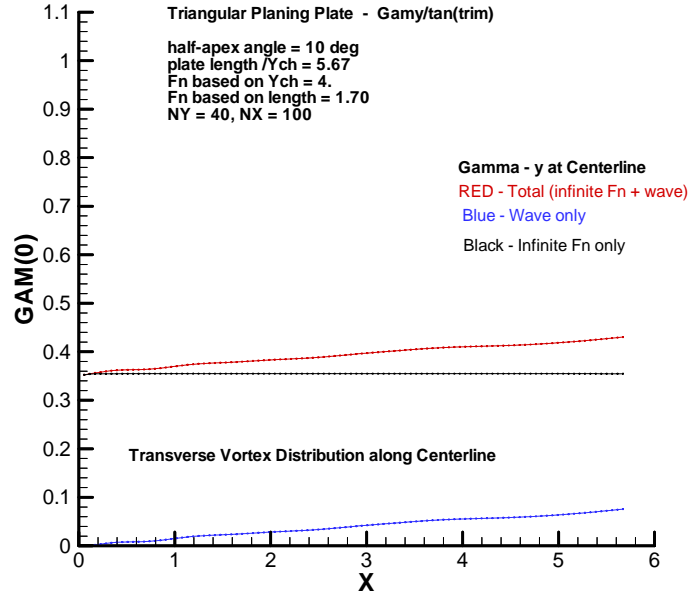


Figure 4: $\gamma_y(x,y)$ along plate centerline; total, wave, and infinite F_n distributions.

The infinite F_n vortex strength shown on Figure 4 is constant in x as required by (21) and (22) for a fixed incidence angle. The non-infinite F_n curves show wave effects, but no centerline singularity.

Figure 5 is a plot of the wave lift coefficient per unit trim-tangent versus F_n for the same 10 deg plate. Mauro's asymptotic form: $C_{LW}/\tan(\text{trim}) = .664\nu$ for high F_n , has been added; ν is the dimensionless wave number: $\nu = \frac{1}{2} \left(\frac{L}{Y_{ch}} \right) \frac{1}{F_{nL}^2}$. The "wave lift coefficient" on Figure 5 is the difference between the total and the infinite F_n C_L from (31), using the corresponding γ_y and γ_{Iy} .

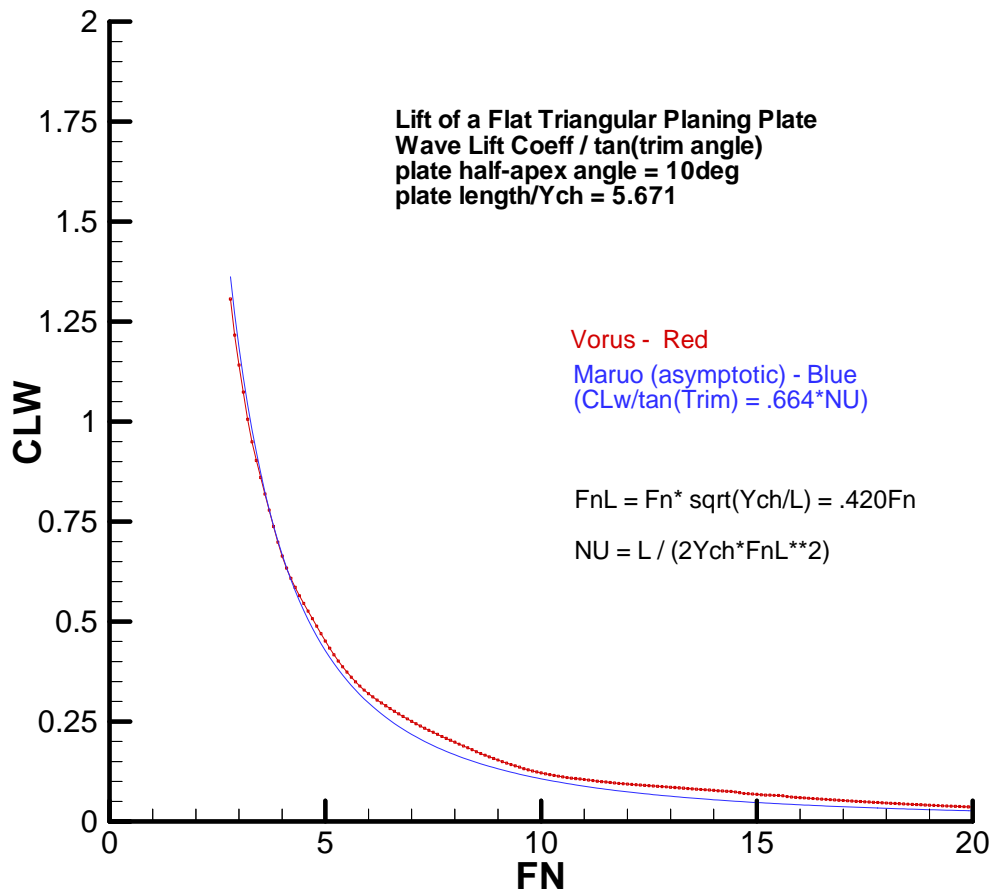


Figure 5: Wave CL versus beam F_n for Half-Apex Angle = 10 deg, Maruo and Vorus Comparison

The Vorus calculation is slightly higher than Maruo for the 10 degree plate, Figure 5, over most of the range, but asymptotes correctly to zero wave resistance in the high F_n limit. The Vorus calculation is also less restrictive than the original Maruo, theoretically. However, it should be noted that below a length F_n of about 1., which corresponds to a half-beam F_n of about 2.5 for the 10 deg plate, both methods begin to lose theoretical validity. The Mauro curve continues climbing indefinitely for reducing F_n because of the simplicity of its high F_n asymptotic construction. The Vorus curve begins to oscillate at F_n much lower than the lower limit shown on Figure 5. It should be recognized, however, that planing craft F_n are not as low as 2.5 (or F_{nL} of unity) at design speed. Caution would be required, however, in applying the theory to semi-planing systems, which are currently of some interest in the field.

This same comparison for a less slender plate, with a half-apex angle of 15 degrees, is shown on Figure 6. The curves are shifted to lower F_n because of the broader transom

beam of the 15 degree wedge. They are otherwise very similar. In fact, if plotted versus wave number the 10 and 15-degree wedge C_{LW} curves exactly overlay.

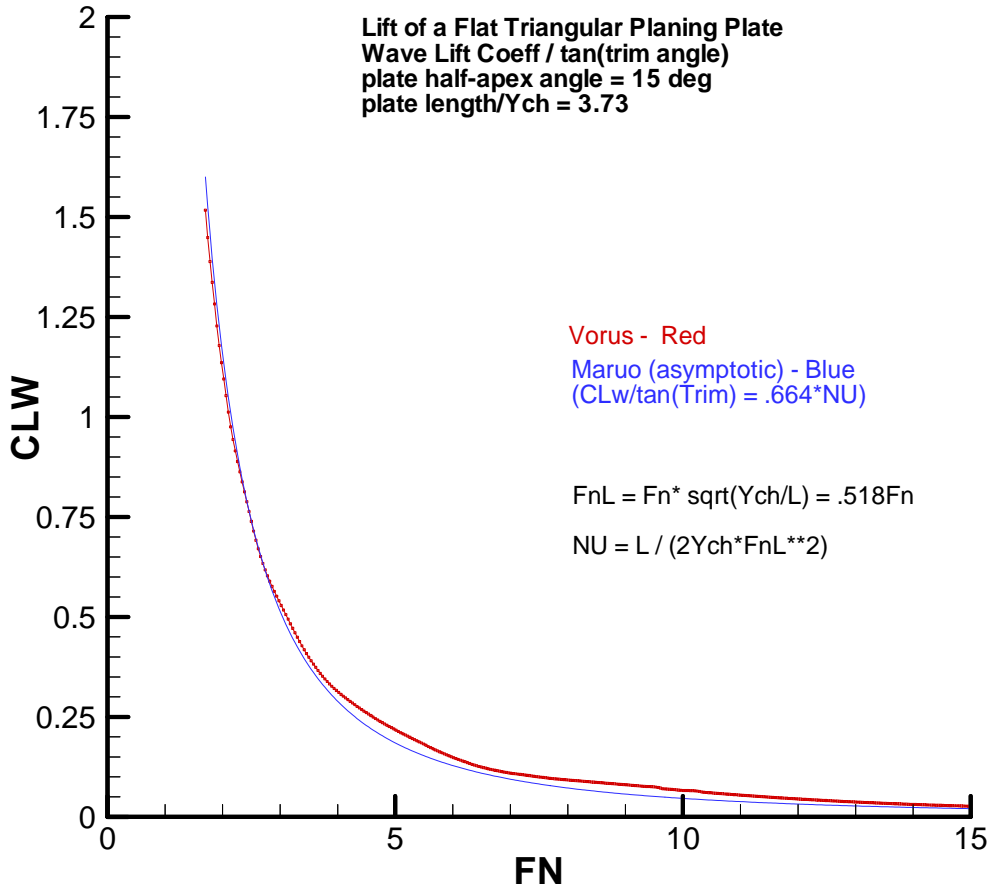


Figure 6: Wave CL versus beam F_n for Half-Apex Angle = 15 deg, Maruo and Vorus Comparison

This is shown on Figure 7, which is a plot versus wave number of the total lift coefficient divided by the infinite- F_n lift coefficient. In this presentation the ratio must go to unity as F_n increases, which corresponds to decreasing v , as wave effects diminish to zero in the limit. The calculation is plotted for both the 10 and 15 degree half-apex angle wedges, which are clearly the same in wave number space. The Maruo asymptotic formula for wedges, as well as data points from the Tuck(1975) graph, are added on Figure 7. The Mauro asymptotic result is just a straight line, linear with wave number, by the formula on the figure.

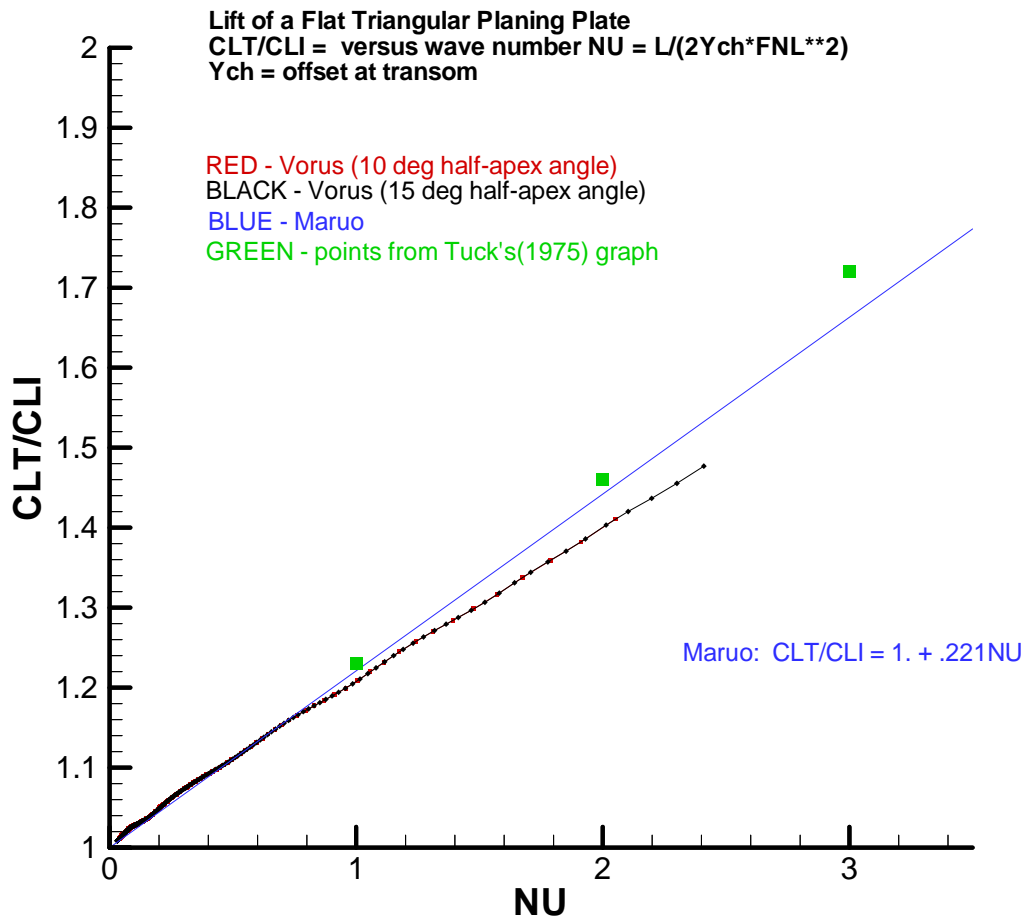


Figure 7: Ratio Total CL to Infinite Fn CL versus Wave Number, 10 and 15 deg plates, Maruo, Vorus, and Tuck Comparison

The reasons for the different trends of the Vorus and Tuck predictions of Figure 7 are not known. It is possible that the singularity suppression treated in the Appendix is not fully effective. But Tuck did express some lack of confidence in his numerical analysis, and the plate centerline singularity in pressure that he claimed actually seems not to be present. Maruo(1967) is difficult and challenging theory to apply practically, as all have found. Further study, focusing on theoretical/numerical sensitivity testing, would be required to verify the Vorus implementation. However, the work proceeds here on the basis that the theory and code developed are capable of providing a meaningful indication of the effects gravity waves on the planing hydrodynamics of actual craft.

Analysis

The theory and code assembled and evaluated in the preceding example of a flat triangular planing plate is now applied in a practical example to predict importance of gravity in the hydrodynamics of actual planing craft. For this purpose, the lines the US

Navy 9300 Series NSW RHIB were approximated. The principal characteristics of the NSW RHIB are listed in Table 1, and Figure 8 is a rendering of its bottom shape.

Table 1 Principle Characteristics of 10m 9300 Series NSW RHIB

Item	Data
Length:.....	10-meters (32.8 ft)
Upper Chine Beam at Transom	2.59-meters (8.4 ft)
Lower Chine Beam at Transom:.....	2.13-meters (6.98 ft)
Light condition displacement:.....	6939 kg (15,300 lbs)
Full load displacement:.....	8800 kg (19,400 lbs)
LCG full load:.....	3.085-meters fwd transom/keel intersect (10.12 ft)
Design Speed	40 knots
Propulsion:.....	Cummins Engine Co. Twin 400 HP Cummins 6CTA8.3 M2 Diesel Engines, Medium continuous duty rating
Marine Waterjet	Hamilton 291

The dynamic system is treated as two degree-of-freedom, to be equilibrated at given speed in calm water. The two degrees of freedom are trim angle, α_T , and transom draft, H_T . The geometry is handled here just as in the non-linear, but zero gravity, code VsSea (VsSea is three DOF, including surge):

- 1) Fit the keel upset from the baseline $Z_k(x_0)$ in $0 \leq x_0 \leq L_{max}$, where L_{max} is the full boat length.
- 2) Given a trial trim angle and transom draft find the intersection of the plane $z = 0$ with the keel. This establishes the running waterline length, consistent with slender body theory (no hydrodynamic disturbance forward of the entry point).
- 3) Discretize the wetted x-axis: $0 \leq x \leq L$, where L is the running waterline length (Figure 1).
- 4) Fit the chine offset, $Y_c(x)$ and deadrise angle $\beta(x)$ in x . The calm-water wetted region of the 10MRB bottom, Figure 8, has minimal transverse camber, so the deadrise angle is only a function of x in this analysis.

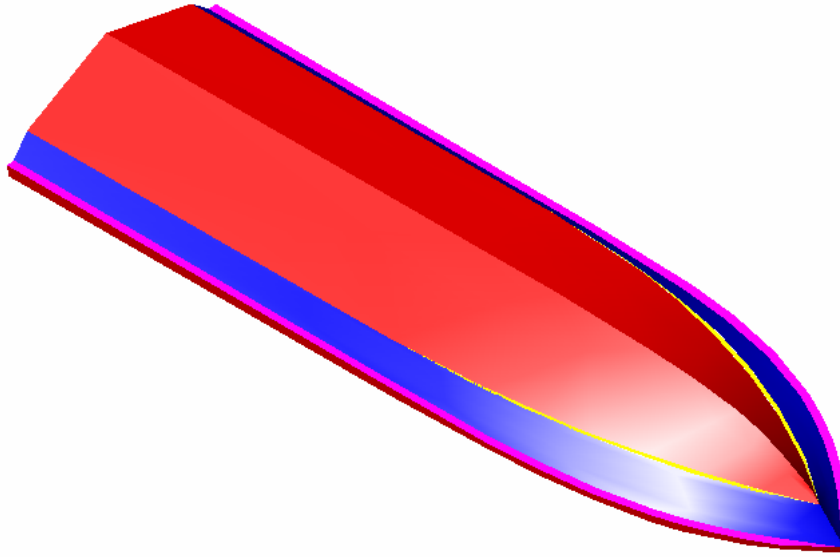


Figure 8: Rendered Drawing of the 10MRB Bottom

- 5) Determine the waterline offset, $Y(x)$. For this purpose first calculate the keel-to-water surface distance: $Z_{wl}(x) = H_T - (L - x) - Z_k(x)$. $Z_{wl}(0) = 0$ by Figure 1. Then:

$$Y(x) = \frac{\pi}{2} J[\beta(x)] Z_{wl}(x) / \tan[\beta(x)] \quad x < x_{cw}$$

$$Y(x) = Y_c(x) \quad x \geq x_{cw}$$
(34)

x_{cw} in (34) is the chine-wetting point, beyond which the wetted offset is the chine offset $Y_c(x)$. x_{cw} is actually determined by the condition (34), with the computation commencing downstream from $x = 0$.

$J[\beta(x)]$ in (34) is the reduction factor from Vorus(1996) for the Wagner wetting factor of $\pi/2$.

- 6) Construct the distribution of hull surface slopes, $z_{0x}(x,y)$:

$$z_{0x}(x,y) = \tan(\alpha_T) - Z_{kx}(x) - \bar{y}Y(x)\beta_x(x) / \cos^2[\beta(x)]$$
(35)

Note in (35) that Z_{kx} and β_x are both negative in value for normal boat geometry.

At this point the complete input data for performing the analysis is provided by L , $Y(x)$ and $z_{0x}(x,y)$ constructed as above. An iteration is performed on trim and transom draft to

achieve equilibrium of weight and longitudinal weight center, starting with assumed trial values at a selected boat speed. The weight of the 10MRB used in the analysis is $\Delta = 19,000\text{lbs}$ (8,613kg) and $X_{CG}/Y_{ch} = 2.9$. The chine half-beam, $Y_{ch} = 1.064\text{m}$. The 19,000 lb weight used in the analysis is slightly less than the design full load displacement listed in Table 1, but is the trial weight of the vessels reported in the NSW report, Najarian (1994). The lift coefficient that must be developed at speed U, along with X_{CG} , is therefore:

$$C_{Lreq} = \frac{\Delta}{\frac{1}{2}\rho U^2}, \text{ with U being craft speed.} \quad (36)$$

The 10MRB has a maximum design speed of 40 knots (Table 1).

This lift coefficient, (36), is composed of the hydrodynamic components of induction, spray, and waves, plus buoyancy. The hydrostatic buoyant lift is taken as that relative to the planing waterline, $Z_{wl}(x)$.

The theory assembled for this analysis reflects the full range of relevant drag sources: induced drag, spray drag, and wave drag, by the Vorus/Maruo analysis, and viscous drag. As is usual, the viscous drag is approximated from the ITTC flat plate friction-line, SNAME (1988), for the planing wetted surface area and at the boat Reynolds number.

The lines of the 10MRB, Figure 8, are indeed quite simple, with minimal variations of chine offset, keel upset and deadrise angle over the wetted length L. The curve fits of these distributions, as required at 1) and 4), are shown on Figures 9, 10, and 11 for equilibrium at an arbitrarily selected boat speed of 34 knots. These distributions imply lines that are almost invariant from cylindrical over the wetted contour, at least in the upper speed range.

This can be confirmed from the plot of the running body plan, Figure 12, constructed collectively from the three distributions at the 100 Nx-stations over the wetted length, 0 to L. The slight deadrise angle reduction in the stem just aft of entry, seen on Figure 11, is hardly discernable on the wetted lines. Both the keel upset and waterline offset are constant with x on these figures, and also over much of the speed range. This can be confirmed from Figures 9, 10, and 11.

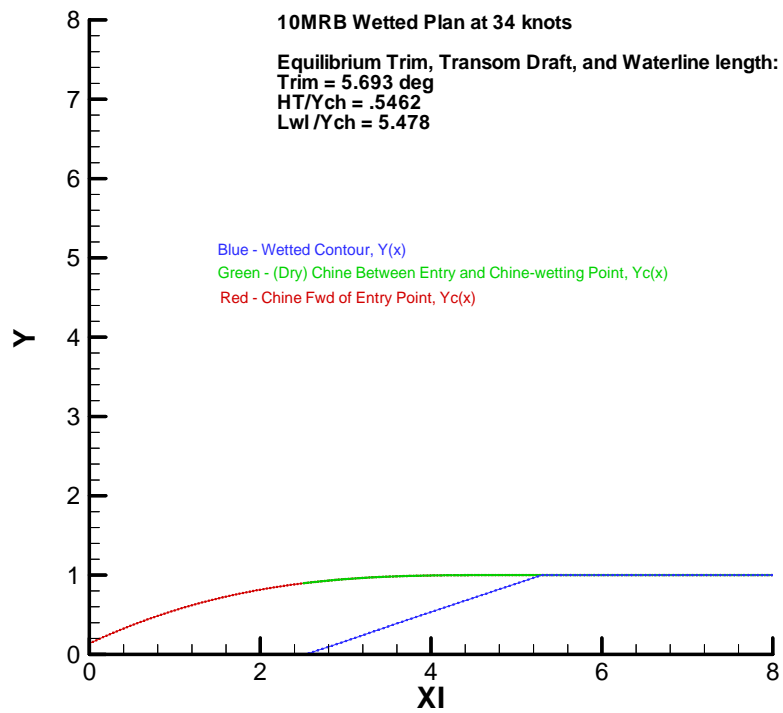


Figure 9: Chine Offset Configuration at 34 knot Equilibrium

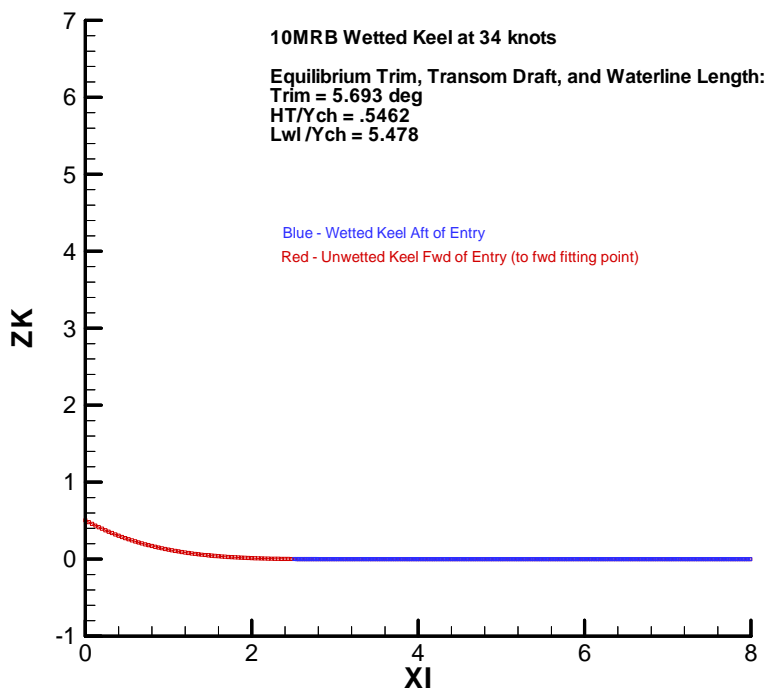


Figure 10: Keel Upset Distribution at 34 knot Equilibrium

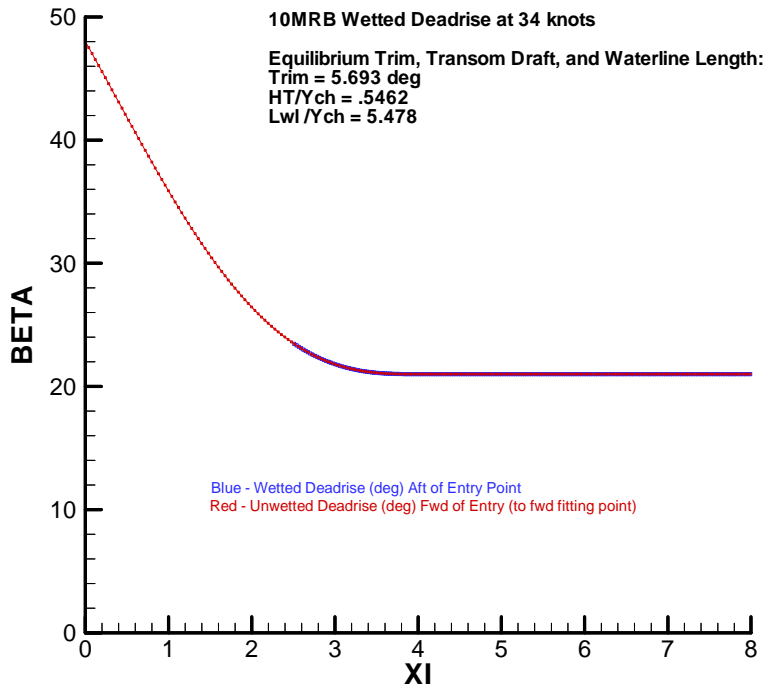


Figure 11: Deadrise Angle Distribution at 34 knot Equilibrium

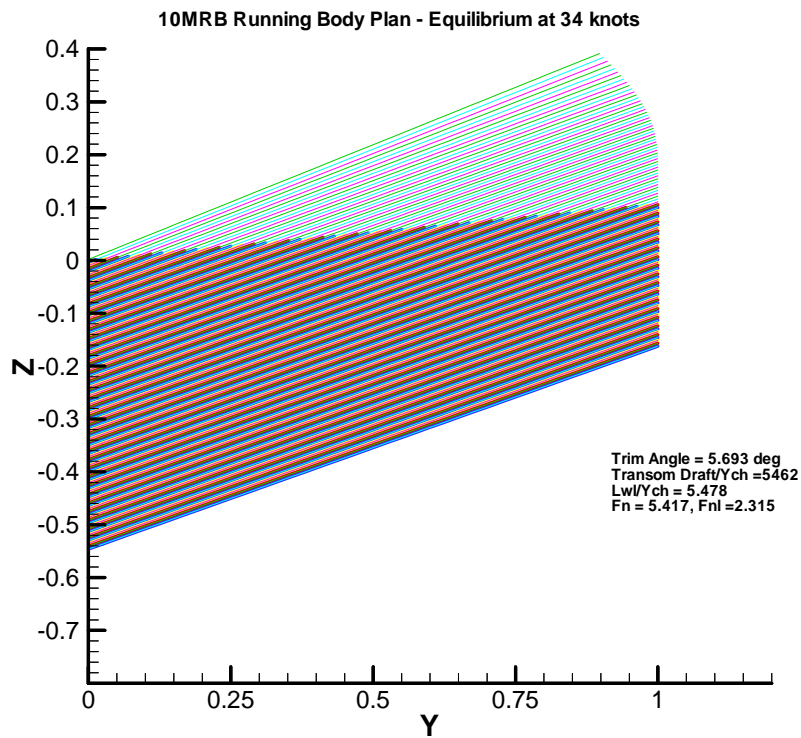


Figure 12: Body Plan at 34 knot Equilibrium (non-zero gravity)

Contribution of Wave-making

Figure 13 is a plot of equilibrium trim and draft versus speed, as predicted by several different methods, in addition to Vorus/Maruo

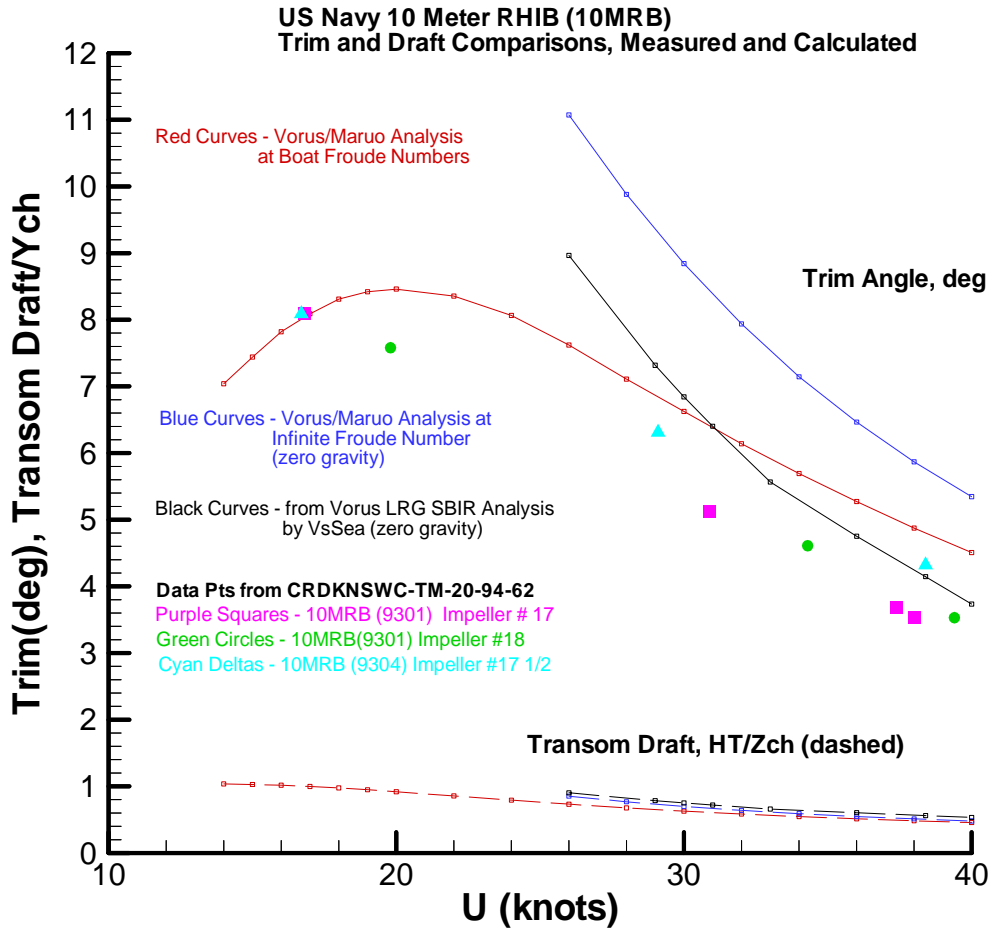


Figure 13: Equilibrium Trim and Draft versus Boat Speed

The red curves on Figure 13 are the Vorus/Maruo (EDITH-h4)² boat trim and transom drafts computed all the way down to 14 knots. At that point ($Fn = 2.23$, $Fnl = .84$, $v = 5.13$ at 14 knots) ill-conditioning of the high Froude number theory begins to develop with further reduced speed. The blue curves on Figure 13 correspond to the infinite Fn analysis via (21) to (23), and the black curves are from the VsSea (EDITH-h1) program, also at infinite Fn .

2 – EDITH (Engineering Development in Theoretical Hydrodynamics) - a system of computer codes and engineering procedures assembled and developed for practical application of theoretical hydrodynamics.

Figure 13 displays some interesting and provocative results:

- 1) It would be thought that the two zero-gravity theories should be closer together. However, the Hamilton water-jet inlet design of the 10MRB is thought to effectively produce a trim-tab effect from a downward-slanting surface extending from the end of the screen to the inlet trailing edge. It was modeled in previous analysis as a trim tab with 10 degrees down angle relative to the boat keel-line aft. Furthermore, the angle on the transom of 10MRB is angled-aft 5 degrees, which further adds to stern lift and bow-down moment on the craft. The boat also has lifting strakes, which produce more lift aft than forward. All three of these effects were included in the non-linear VsSea analysis, but not in the Vorus/Maruo calculation, and all three tend to reduce boat trim. This is believed to largely explain the trim differences in the two zero gravity cases of Figure 13³.
- 2) Note that if the secondary stern lift effects had been included in the Vorus/Maruo analysis, then the almost constant shift observed with the zero gravity curves would be expected to shift the non-zero gravity curve on Figure 13 down by approximately the same amount. This would be in the upper speed range where trim tabs are effective.
- 3) The Vorus/Maruo calculation does capture the resistance hump predicted to peak at 20 knots. This is completely out of reach of the zero gravity theories, and any other rational theories for that matter, and it is important.

The corresponding running wetted-lengths and Froude numbers versus speed are plotted on Figure 14. At the higher speeds the running wetted length by Vorus/Maruo lies between the zero gravity calculations, as would be expected by comparison of the trims on Figure 13. However, on that basis the wetted length might be expected to be closer to the VsSea prediction. The reason that it is not is the lower transom draft predicted with non-zero gravity, Figure 13. Transom draft reduction is an important consideration that is often ignored in the thinking of planing hull efficiency. In consideration of trim alone it is clear that pressure drag increases directly with trim and viscous drag increases inversely with trim. But minimum drag is achieved with both low trim and low transom draft, in combination. The lower trim results in both reduced induced, wave, and spray drag and the shorter waterline with the lower transom draft reduces viscous drag. In connection with Figures 13 and 14, this favorable effect of low trim and low transom draft can only be from extra stern lift due to the boat generated waves, which grows aft from the bow. But what about the wave drag that is added?

Figure 15 addresses this question, and is also at the root the essential objective of the work as posed in the **Introduction**: The objective of this paper is to shed light on the general importance, or unimportance, of wave-making with boats developing significant hydrodynamic lift, versus those that develop mainly displacement (buoyant) lift.

3 – VsSea employs consistent nonlinear hydrodynamics in the zero gravity theory, by Vorus (1996), but the contribution of that difference to the comparative results presented here has not been assessed.

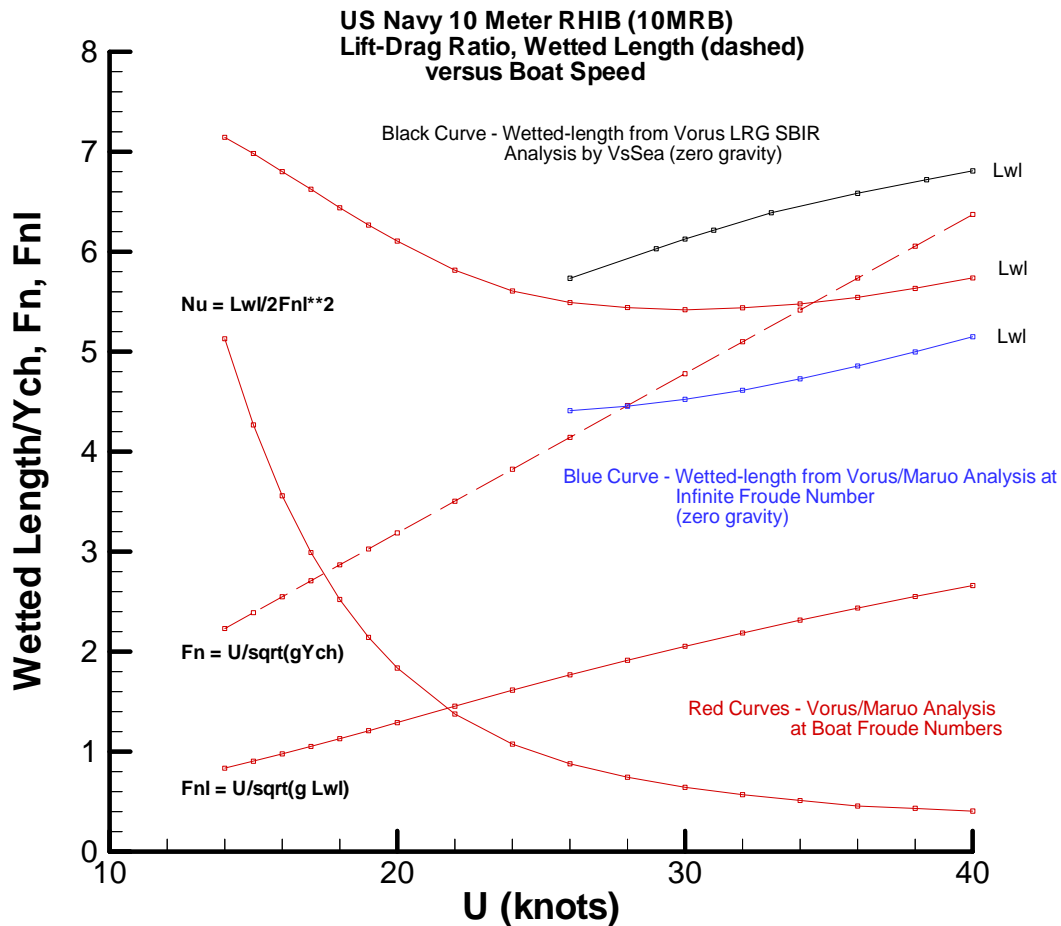


Figure 14: Equilibrium Wetted-Length and Froude Number versus Boat Speed

The lift is constant in Figure 15, corresponding to the boat displaced weight, so that L/D variations are a direct reflection of variations in drag. The most remarkable aspect of Figure 15 is that the gravity free-surface effects are predicted to *reduce* overall drag relative to the zero gravity predictions. This is in spite of the lower trim, which usually results in longer wetted lengths and increased viscous drag. This is as discussed under Figure 14, in connection with the lower trim and lower transom draft in combination as exhibited on Figure 13. It must be kept in mind that planing boat resistance is a strong function of boat trim and draft, which both vary strongly with all of the hydrodynamic loads. This is different from the case of displacement craft. The specific manifestation at 34 knots is seen on Figure 16, which plots the predicted $Cl(x)$ and $Cd(x)$ over the boat wetted-lengths for the two cases with gravity and without by the Vorus/Maruo analysis. First of all, the waterline length differences of Figure 14 are evident. Further, the areas under the two $Cl(x)$ curves are the same.

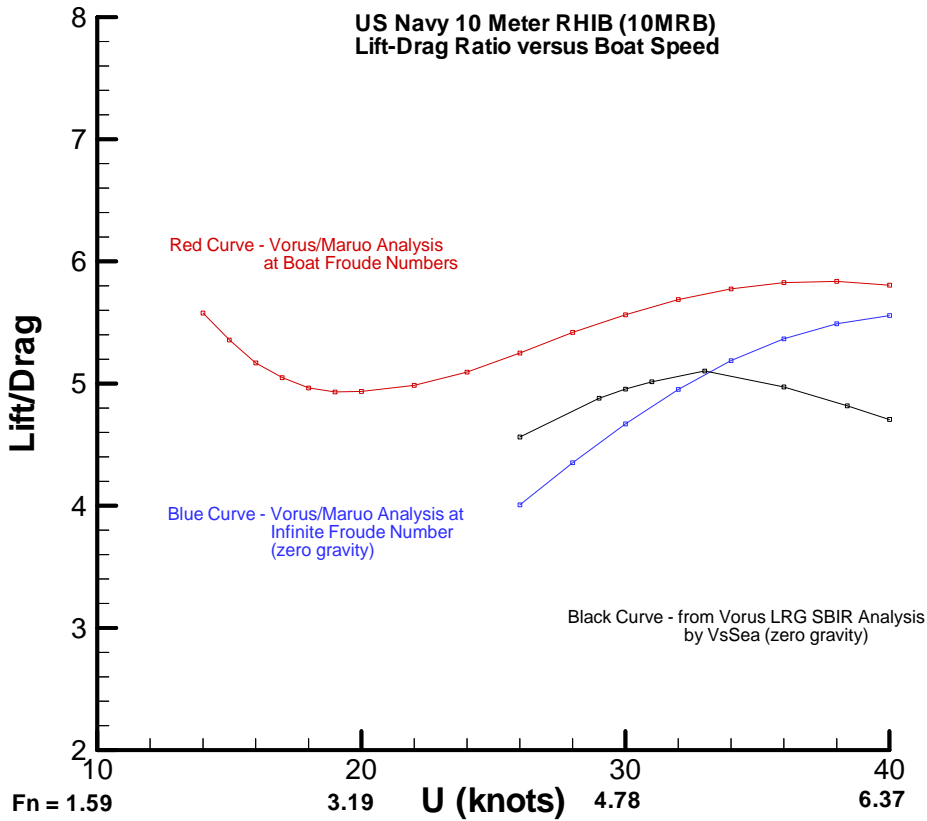


Figure 15: Equilibrium Lift-Drag Ratios versus Boat Speed

The large drop in lift is at the chine-wetting point, (34). It is a characteristic of linear, zero-gravity slender-body theory that once the geometry has ceased changing with x downstream, the lift is entirely bouyancy and the drag is entirely viscous. This is at the chine-wetting point x_{cw} for the blue zero gravity curves on Figure 16.

The areas under the drag curves is slightly larger for the zero gravity case. This is because the lift aft, due primarily to waves, has lifted the stern of the boat, reduced the transom draft and flattened the trim to produce a lower total drag, even though the wave drag is a non-zero addition. The total wave drag coefficient for this case is $CD_w = .00808$ out of a total $CD = .0842$. For equilibrium at infinite Fn , the wave drag is, of course, zero, but the total drag, being the sum of the induced, spray and viscous components and represented by the area under the blue drag curve on Figure 17, is $CD = .0938!$

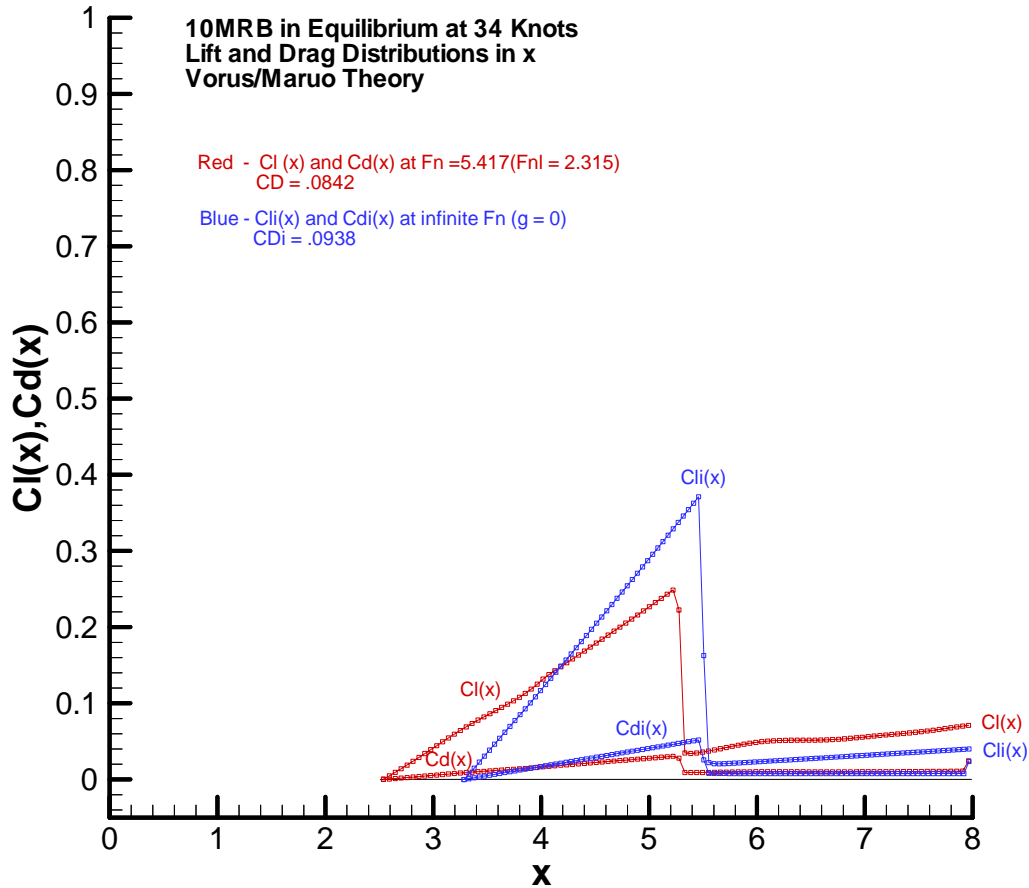


Figure 16: Lift and Drag Coefficient Distributions at 34 knots

To check for consistency, the same calculation as represented by Figure 16 was checked at 26 knots, which is the lowest zero gravity calculation performed. Figure 17 is the wetted body plan for equilibrium with non-zero gravity, the data points of which can be confirmed to check with Figures 14 and 15.

The lift and drag comparison, Figure 18, is even more vividly demonstrated here as all of the components are larger. But the general conclusion is the same. Because of aft loading by the boat-generated wave system producing hull rise and trim reduction, the total resistance with gravity is predicted to be lower than the boat drag at equilibrium with no wave generation. Note again that there is a positive wave resistance component, but it is just an additive component in an overall drag that is reduced with wave making.

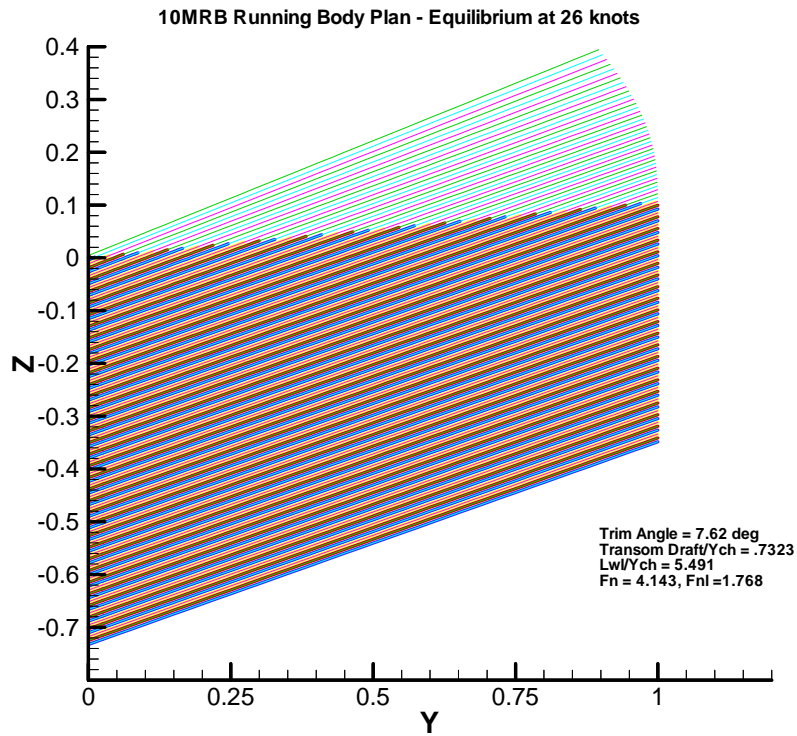


Figure 17: Body Plan at 26 knot Equilibrium (non-zero gravity)

Conclusion

Linear planing theory applied to a modern military craft has shown a positive wave resistance component but a reduced overall drag relative to the prediction of the usual planing model that assumes infinite Froude number (no gravity waves).

Some care must be exercised with drawing conclusions on the basis of the limited investigation conducted here. However, the extended Maruo theory does check well in the numerical limit with asymptotic results produced by Maruo himself, and its application to a modern US Naval craft for which trim data is available is quite positive, even down to “hump level” Froude numbers.

In retrospect, the prediction that the net effect of wave-making on boat drag is a drag *reduction* should not be viewed as too implausible. Theory indicates that many of the physical performance characteristics of planing craft are consistently opposite those of displacement vessels.

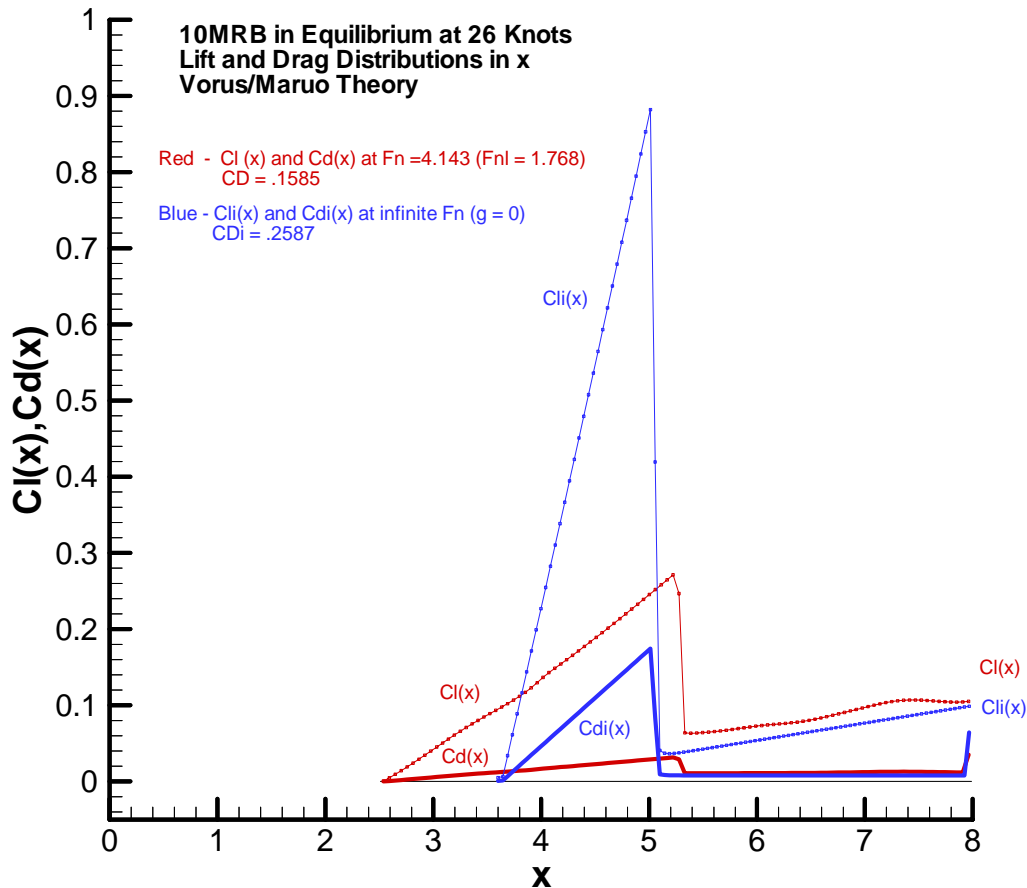


Figure 18: Lift and Drag Coefficient Distributions at 26 knots

For example, planing craft rise in calm, shallow water, and resistance drops with the consequent lower wetted surface area. But displacement vessels sink, and resistance increases. This is because, for the planing craft, the positive craft bottom pressure needed for hydrodynamic lift is amplified by diffraction flow off the water bottom. For displacement vessels, on the other hand, there is increased tangential hull surface velocity, and decreased pressure, due to the increased “squeeze” in the bottom-to-bottom gap under the displacement vessel.

As another example, planing craft have been observed to experience reduced mean resistance in traversing ambient waves, whereas displacement vessels have added resistance in waves. For the planing boat impacting in the wave system, there is more impact up than down, so the boat rises in the wave system in the mean over time and its mean resistance is again reduced by the reduction in mean wetted surface. The planing boat is extracting energy from the wave system in reducing its power requirement, and the residual ambient waves are consequently reduced in the wake of the boat. For the displacement vessel the wave impacts are more axial, and result in a mean added drag

through the nonlinear interaction; a wave system of increased height is produced in the wake the displacement vessel.

Here it is offered that a planing craft can have reduced resistance in calm-water due to its own wave system lifting the craft, reducing the wetted surface, and producing a more favorable running attitude. Whereas the displacement craft, whose running attitude is not so dependent on the hydrodynamic loads developed, and vice-versa, clearly experiences increased overall drag due to wave-making.

The suggestion is that, if true, this characteristic could be factored to advantage into the design of high-speed semi-planing/semi-displacement ships, with increases in power required to generate some hydrodynamic planing lift at least partially offset by achieving a running attitude resulting in reduced resistance relative to the fully displacement alternative.

With regard to the original question, as reflected in the title of this paper, it appears from the work done here that gravity and the inherent wave-making can be significant in planing, in deference to the almost universal assumption of zero gravity in planing boat hydrodynamic analysis!

Acknowledgement: The author wishes to express his appreciation to the ONR Naval Engineering Modeling and Optimization Program (NEMO) for funding the work presented here and to the Contractor, ATI, for its management role.

References

- Cole, S. 1988 A simple example from flat ship theory. *Journal of Fluid Mechanics*, **189**
- Gradshteyn and Ryzhik 1965 *Table of integrals, series, and products*. Academic Press, New York
- Lewis, E. 1988 Chapter 5, Resistance, *Principles of Naval Architecture*, SNAME, Jersey City, NJ
- Najarian, R. 1994 Developmental test and evaluation, NSW 10 meter inflatable boat (RIB). CRDKNSWC-TM-294-62, July
- Maruo, H. 1967 High and low-aspect ratio approximation of planing surfaces. *Schiffstechnik*, **72**.
- Michell, J. 1898 The wave resistance of a ship. *Philosophical Magazine*, **5**, 45
- Tuck, E. 1975 Low-aspect ratio flat-ship theory. *Journal of Hydronautics*, **9**, 1, January

Tulin, M. 1957 The theory of slender surfaces planing at high speeds. *Schiffstechnik* **4**.

Von Karman, T. 1929 The impact of seaplane floats during landing. NACA TN 321
Washington, D.C., Oct.

Vorus, W. 1996 A flat cylinder theory for vessel impact and steady planing resistance.
Journal of Ship Research, **40**, 2, June.

Wagner, H. 1932 Uber stoss-und gleitvorgange an der oberflache von flussigkeiten.
Zeitschrift fur Angewandte Mathematik und Mechanik, **12**, 193, Aug.

Appendix - Singularity Suppression

The I_{λ}^{-} integral of equations (7) and (8) of the text has a higher order singularity that causes trouble numerically:

$$I_{\lambda}^{-} = \int_{\lambda=0}^{\infty} \sin \frac{\sqrt{\lambda}}{F_n} (x - \xi) \Big|_{\xi=\xi_i}^{\xi_{i+1}} \sin \lambda Y(x) (\bar{y} - \eta) \Big|_{\eta=\eta_j}^{\eta_{j+1}} e^{\lambda z} \frac{d\lambda}{\sqrt{\lambda}} \quad (1A)$$

If z is here set to zero in (1A) as it was in I_{λ}^{+} at (9) and the same integration performed, a similar result to (9) in terms of the Fresnel Integrals is obtained, but with the negative sign in the a -parameter of (10). That is:

$$I_{\lambda}^{-}(x, \bar{y}, \xi, \eta) \Big|_{z=0} \equiv I_{\lambda 0}^{-} = \operatorname{sgn}(\bar{y} - \eta) \sqrt{\frac{\pi}{2}} \frac{1}{a_{-}} \left[\cos \left(\frac{b^2}{a_{-}^2} \right) C \left(\frac{b}{a_{-}} \right) + \sin \left(\frac{b^2}{a_{-}^2} \right) S \left(\frac{b}{a_{-}} \right) \right] \quad (2A)$$

with,

$$a_{-}(x, \bar{y}, \eta) \equiv \sqrt{Y(x) |\bar{y} - \eta|} \quad \text{and,} \quad b = b(x, \xi) \equiv \frac{x - \xi}{2F_n} \quad (3A)$$

The situation of concern with I_{λ}^{-} and $z = 0$ is when x lies some distance downstream of ξ , such that $x \gg \xi$ and $b(x, \xi)$ at (10) is not vanishingly small. Further, when $\bar{y} = \bar{y}_j$ lies between η_j and η_{j+1} in the j^{th} segment in the summation at (7), $a_{-} = O(\Delta\eta_j)^{1/2}$ so that the argument of the Fresnel integrals in $I_{\lambda 0}^{-}$ is large. In this case $I_{\lambda 0}^{-}$ becomes in the limit:

$$I_{\lambda 0}^{-} \rightarrow -\frac{1}{2} \sqrt{\pi} \frac{1}{\sqrt{Y(x) \Delta\eta_j / 2}} \cos \left[\frac{b^2}{Y(x) \Delta\eta_j / 2} - \frac{\pi}{4} \right] \quad (4A)$$

with $\Delta\eta_j \equiv \eta_{j+1} - \eta_j$.

It is therefore clear from (4A) that I_{λ}^{-} evaluated with $z = 0$ is characterized by a divergent oscillation for $\Delta\eta_j$ small and $x - \xi$ increasing. This singularity was discussed by Tuck(1975), but he was not very satisfied with the precision of his treatment.

Singularity Suppression

The integration I_{λ}^{-} with $z \neq 0$, (1A), can be preformed in terms of the exponential forms of the trigonometric functions. First redefine for notational convenience:

$\alpha_1 \equiv Y(x)(\bar{y} - \eta)$ and $\alpha_2 \equiv 2b = \frac{x - \xi}{F_n}$. Then write I_{λ}^{-} as the four term superposition:

$$I_{\lambda}^{-} = \sum_{k=1}^4 I_{\lambda k}^{-} \quad (5A)$$

Each of the four terms in (5A) is a product of the exponentials formed in the integrand of (1A). These terms integrate by Gradshteyn and Ryzik(1965), 3.322.2, as:

$$I_{\lambda 1}^{-} = -\frac{1}{4} \sqrt{\frac{i\pi}{\alpha_1 + iz}} e^{\frac{-i\alpha_2^2}{4(\alpha_1 + iz)}} \left[1 - \Phi\left(\frac{-i\alpha_2\sqrt{i}}{2\sqrt{\alpha_1 + iz}}\right) \right]$$

$$I_{\lambda 2}^{-} = \frac{1}{4} \sqrt{\frac{-i\pi}{\alpha_1 - iz}} e^{\frac{i\alpha_2^2}{4(\alpha_1 - iz)}} \left[1 - \Phi\left(\frac{-i\alpha_2\sqrt{-i}}{2\sqrt{\alpha_1 - iz}}\right) \right]$$
(6A)

$$I_{\lambda 3}^{-} = \frac{1}{4} \sqrt{\frac{i\pi}{\alpha_1 + iz}} e^{\frac{-i\alpha_2^2}{4(\alpha_1 + iz)}} \left[1 - \Phi\left(\frac{i\alpha_2\sqrt{i}}{2\sqrt{\alpha_1 + iz}}\right) \right]$$

$$I_{\lambda 4}^{-} = -\frac{1}{4} \sqrt{\frac{-i\pi}{\alpha_1 - iz}} e^{\frac{i\alpha_2^2}{4(\alpha_1 - iz)}} \left[1 - \Phi\left(\frac{i\alpha_2\sqrt{-i}}{2\sqrt{\alpha_1 - iz}}\right) \right]$$

where Φ is now the error function, erf(arg).

Write the binomial $\alpha_1 \pm iz$ appearing in (6A) as:

$$\alpha_1 \pm iz = \alpha_1 \left(1 \pm \frac{iz}{\alpha_1} \right) \quad (7A)$$

Next consider z selected as a value such that $\frac{z}{\alpha_1} \ll 1$. Taking proper care with the

branch-cuts in (6A), the dominant multiplicative factor common to all the integrals (6A) arises from the exponential term multiplying all four. With this selection of z small, the four components of (6A) become, Gradshteyn and Ryzik (1965), (8.25):

$$I_{\lambda k}^{-} = I_{\lambda k 0}^{-} e^{\frac{z}{4} \left(\frac{\alpha_2}{\alpha_1} \right)^2} = I_{\lambda k 0}^{-} e^{z \left(\frac{b}{Y(x)(\bar{y} - \eta)} \right)^2} \quad k = 1, \dots, 4; \quad z < 0 \quad (8A)$$

where $I_{\lambda k_0}^-$ are the functions (6A) with $z = 0$, which correspond in superposition to (2A). The argument of the exponential factor in (8A) is large for \bar{y}_j in η_j, η_{j+1} , whereas the imaginary term $\frac{z}{\alpha_1}$ in (7A) is small, by prescription. Retain this exponential factor as the lowest order function of z . This gives the following result at (6A), hence (2A) via (5A):

$$I_{\lambda}^-(x, \bar{y}, \xi, \eta) \equiv \text{sgn}(\bar{y} - \eta) \sqrt{\frac{\pi}{2}} \frac{1}{a_-} \left[\cos\left(\frac{b^2}{a_-^2}\right) C\left(\frac{b}{a_-}\right) + \sin\left(\frac{b^2}{a_-^2}\right) S\left(\frac{b}{a_-}\right) \right] e^{z \left(\frac{b}{Y(x)(\bar{y} - \eta)} \right)^2} \quad (9A)$$

The numerical convergence is now provided by the exponential factor; z is selected so that, as required by (7A), $\frac{|z|}{Y(x)|\bar{y} - \eta|} \ll 1$. The maximum value occurs at the minimum of $Y(x)\Delta\eta_j/2$ such that z can be taken arbitrarily as $|z| \ll Y(x) \min(\Delta\eta_j)/2$ for computational purposes; a value of $z(x) = -\varepsilon Y(x) \min(\Delta\eta_j/2)$ with ε on the order of $\varepsilon = .1$ to $.2$ is found to be appropriate. The decaying exponential in (9A) then provides the needed override of the higher order singularity locally and the required convergence.

The large argument limiting term, (4A), becomes with this factor retained:

$$I_{\lambda}^- \rightarrow -\frac{1}{2} \sqrt{\pi} \frac{1}{\sqrt{Y(x)\Delta\eta_j/2}} \cos\left[\frac{b^2}{Y(x)\Delta\eta_j/2} - \frac{\pi}{4} \right] e^{-\varepsilon \left(\frac{b^2}{Y(x)\Delta\eta_j/2} \right)} \quad (10A)$$

with $\frac{b^2}{Y(x)\Delta\eta_j/2} \gg \varepsilon$ for $b = O(1)$.

z is effectively being placed just below the $z = 0$ plane for evaluation near the y -singularities. This is a not uncommon de-singularization concept for singular integral equations.

This convergence factor can actually be applied to both sets of terms originating at (5) of the text without any loss of function. For $\bar{y} + \eta$ or for $\bar{y} - \eta$ with $\bar{y} \neq \bar{y}_j$, or for $b \rightarrow 0$, the exponential argument is then small, such that minimum reduction occurs where none is needed.